



A Systematic Study of Superluminous Supernova Light-curve Models Using Clustering

E. Chatzopoulos^{1,2}  and Richard Tuminello¹

¹ Department of Physics & Astronomy, Louisiana State University, Baton Rouge, LA 70803, USA; chatzopoulos@phys.lsu.edu

² Hearne Institute of Theoretical Physics, Louisiana State University, Baton Rouge, LA 70803, USA

Received 2019 January 25; revised 2019 February 25; accepted 2019 February 25; published 2019 March 26

Abstract

Superluminous supernova (SLSN) light curves exhibit superior diversity compared to their regular-luminosity counterparts in terms of rise and decline timescales, peak luminosities, and overall shapes. It remains unclear whether this striking variety arises due to a dominant power input mechanism involving many underlying parameters or due to contributions by different progenitor channels. In this work, we propose that a systematic quantitative study of SLSN light-curve timescales and shape properties, such as symmetry around peak luminosity, can be used to characterize these enthralling stellar explosions. We find that applying clustering analysis to the properties of model SLSN light curves, powered by either a magnetar spindown or a supernova ejecta–circumstellar matter interaction mechanism, can yield a distinction between the two, especially in terms of light-curve symmetry. We show that most events in the observed SLSN sample with well-constrained light curves and early detections are strongly associated with clusters dominated by circumstellar interaction models. Magnetar spindown models also show association at a lower degree but have difficulty in reproducing fast evolving and fully symmetric light curves. We believe this is due to the truncated nature of the circumstellar interaction shock energy input compared to decreasing but continuous power input sources like magnetar spindown and radioactive ^{56}Ni decay. Our study demonstrates the importance of clustering analysis in characterizing SLSNe based on high-cadence photometric observations that will be made available in the near future by surveys like the Large Synoptic Survey Telescope, Zwicky Transient Facility, and Panoramic Survey Telescope and Rapid Response System.

Key words: circumstellar matter – methods: data analysis – stars: magnetars – supernovae: general

1. Introduction

Superluminous supernovae (SLSNe; Gal-Yam 2012, 2018; Moriya et al. 2018b) possess a striking diversity in terms of photometric and spectroscopic properties. SLSNe are often divided into two classes based on the presence of hydrogen (H) in their spectra: H-poor (SLSN-I) and H-rich (SLSN-II) events. In terms of photometry, SLSNe are characterized by reaching very high peak luminosities ($\gtrsim 10^{44} \text{ erg s}^{-1}$) over timescales ranging from a few days to several months. The overall evolution and shape of SLSN light curves (LCs) can significantly vary from one event to another. Some SLSN LCs appear to have a symmetric, bell-like shape around peak luminosity (Barbary et al. 2009; Quimby et al. 2011), while others are highly skewed with a fast rise followed by a slow, long-term decline (Drake et al. 2011; Lunnan et al. 2016). Most SLSNe appear to be hosted in low-metallicity dwarf galaxies similar to long-duration gamma-ray bursts (LGRBs) (Neill et al. 2011; Lunnan et al. 2014).

Several power input mechanisms have been proposed to interpret the extreme peak luminosities and diverse observational properties of SLSNe. Most SLSNe-II show robust signs of circumstellar interaction with a hydrogen medium in their spectra, indicating that effective conversion of shock heating to luminosity can reproduce their LCs (Smith & McCray 2007; Chatzopoulos et al. 2013). SLSNe-I, on the other hand, do not show the usual signatures of circumstellar interaction and are often modeled by magnetorotational energy release due to the spindown of a newly born magnetar following a core-collapse supernova (CCSN) explosion (Kasen & Bildsten 2010; Woosley 2010; Inerra et al. 2013).

Nonetheless, the association between power input mechanism and SLSN type is still ambiguous. The magnetar spindown model is occasionally invoked as an explanation for

SLSNe-II that exhibit P-Cygni $\text{H}\alpha$ line profiles, like SN 2008es, (Kasen & Bildsten 2010; Dessart 2018). On the other hand, circumstellar interaction cannot be completely ruled out for SLSN-I events because H lines may be hidden, due to complicated circumstellar matter geometries (Kleiser et al. 2018; McDowell et al. 2018), details of nonlocal thermal equilibrium line transfer physics in nonhomologously expanding shocked, dense regions still unexplored by numerical radiation transport models (Chatzopoulos et al. 2013; Dessart et al. 2015) or, simply, interaction with a H-deficient medium (Chatzopoulos & Wheeler 2012a; Chatzopoulos et al. 2016; Sorokina et al. 2016). A subclass of SLSNe is found to transition from SLSN-I at early times to SLSN-II of Type IIn at late times indicating late-time interaction adding to the complexity of the problem (Yan et al. 2017).

Breaking the degeneracy between SLSNe powered by magnetar spindown, circumstellar interaction, and other mechanisms will help address a variety of important questions surrounding massive stellar evolution and explosive stellar death: the link between LGRBs and SLSNe, the formation of extremely magnetized stars following CCSNe and their effect on the dynamics of the expansion of the supernova (SN) ejecta, the mass-loss history of massive stars in the days to years prior to their explosion and how their environments affect the radiative properties of their explosion, to name a few.

The advent of automated, wide-field, high-cadence transient surveys like the Panoramic Survey Telescope and Rapid Response System, Pan-STARRS (Kaiser et al. 2002); the Zwicky Transient Facility, ZTF (Bellm et al. 2019), and, of course, the Large Synoptic Survey Telescope, LSST (Ivezic et al. 2008) will significantly enhance the SLSN discovery rate and equip us with more complete photometric coverage that

includes detections shortly after the SN explosion, tightly constraining the LCs of these events.

This work aims to illustrate how well-sampled LCs can be used to unveil the power input mechanism of SLSNe. This is done by quantitatively characterizing several key properties of SLSN LCs such as rise and decline timescales (Nicholl et al. 2015a) and LC symmetry around peak luminosity. Using the power of machine learning and k -means clustering analysis, we are able to distinguish between groups of LC shape parameters corresponding to different power input mechanisms and calculate their association with the properties of observed SLSN LCs.

Our paper is organized as follows: Section 2 presents the observed SLSN LC sample that we use in this work and introduces the LC shape properties that are utilized in our analysis. Section 3 introduces the SLSN power input models adopted to obtain large grids of semianalytic LCs across the associated parameter spaces. Section 4 introduces the k -means clustering analysis method that we employ to characterize observed and model SLSN LCs, and Section 5 details the results of this analysis. Finally, Section 6 summarizes our discussion.

2. Observed SLSN Light-curve Sample

We use the Open Supernova Catalog (OSC; Guillochon et al. 2017) to access publicly available photometric data on a sample of 126 events that are spectroscopically classified as SLSN-I (68% of the sample) or SLSN-II (32% of the sample).

For events with available redshift measurements, we compute pseudo-bolometric LCs using the SuperBol³ code (Nicholl 2018). SuperBol is a user-friendly Python software instrument that uses the available observed fluxes in different filters to fit blackbodies to the spectral energy distribution (SED) of an SN. The resulting pseudo-bolometric SN LCs can also be corrected for time dilation and distance, and converted to the rest frame (K -correction). Using extrapolation techniques, missing near-infrared and ultraviolet (UV) flux can also be accounted for. Subsequently, all rest-frame LCs are translated in time so that $t = 0$ is coincident with the time corresponding to peak luminosity ($t_0 = t_{\max}$) and scaled by the peak luminosity (L_{\max}).

For the purposes of our study, we select a subsample of SLSNe defined by rest-frame LCs with near-complete temporal photometric coverage, which we define as including observed data in the range $L_{\max}/e < L(t) < L_{\max}$ (or $1/e < L(t) < 1$ in the scaled form). Thus, we only focus on SLSN LCs with observed evolution within one e -folding timescale from the peak luminosity, ensuring that our analysis relies only on real data and not approximate, often model-based, extrapolations to explosion time (see Section 2.1). In this regard, our sample selection criterion for LC coverage is similar to that used in Nicholl et al. (2015a; hereafter referred to as N15) but our SLSN sample is larger than their “gold” sample by eight events, due to our inclusion of SLSN-II events and the availability of more SLSN discoveries since their publication. This process leaves us with a reduced sample of 25 SLSNe with well-covered LCs: 21 SLSN-I and 4 SLSN-II events. Table 1 presents the details of the SLSN sample used in our analysis, including the photometric band with the longest (in

time) LC coverage that was used in generating their pseudo-bolometric LC.

2.1. Quantitative Properties of SLSNe LC Shapes

In order to quantitatively constrain the shapes of SLSN LCs, we define the following scaled luminosity thresholds:

1. Primary luminosity threshold: $L_1 = 1.0/e$ or 36.79% of the peak luminosity.
2. Secondary luminosity threshold: $L_2 = 1.0/(0.5e)$ or 73.58% of the peak luminosity.
3. Tertiary luminosity threshold: $L_3 = 1.0/(0.4e)$ or 91.97% of the peak luminosity.

At each luminosity threshold, we can compute a “rise time” to peak luminosity and a “decline time” from peak. As such, we accordingly define the primary, secondary, and tertiary rise (tr_1, tr_2, tr_3) and decline (td_1, td_2, td_3) timescales. It is evident that $t[d, r]_3 < t[d, r]_2 < t[d, r]_1$, and that all of the SLSNe in our selected LC sample have observations that include these timescales. We note that our choice for the primary luminosity threshold and corresponding rise and decline timescales is the same as the one used in N15 to study how closely these timescales correlate with different power input models.

Next, for the sake of quantifying how symmetric an LC is around peak luminosity, we define three corresponding “LC symmetry” parameters: $s_{1,2,3} = tr_{1,2,3}/td_{1,2,3}$. The closer these parameters are to unity, the more symmetric the LC is at the corresponding luminosity threshold. Obviously, to consider an LC as “fully symmetric,” all of the three LC symmetry parameters need to be close to unity. For the purposes of this study, we define a symmetric LC, one that satisfies the criterion $0.9 < s_{1,2,3} < 1.1$. For the remainder of this paper, we refer to the nine ($tr_{1,2,3}, td_{1,2,3}, s_{1,2,3}$) LC parameters as “LC shape parameters.”

We have developed a Python script that fits a high-degree polynomial to the scaled observed LCs of the SLSNe in our sample. This provides us with interpolation between missing photometric data points and an accurate measurement of the LC shape parameters discussed above. An example of such fit is shown in Figure 1 for SN2006, inarguably one of the most well-observed SLSN-II of Type IIn (Smith et al. 2007). In this figure, the light blue horizontal lines show the three luminosity thresholds that were introduced earlier. Based on these thresholds, we find $tr_1 = 41.0$ days and $td_1 = 54.3$ days for this SN, implying primary symmetry $s_1 = 0.76$. The rest of the LC shape parameters for SN2006gy are given in Table 1. Table 2 lists the main LC shape statistical properties of the observed SLSNe-I and SLSNe-II in our sample. The SLSN-II sample only includes four events, thereby preventing us from performing an accurate statistical comparison against the SLSN-I sample to look for potential systematic differences in the two distributions.

Our sample overlaps with that presented in Table 3 of N15 for 11 SLSNe: SN2011ke, SN2013dg, LSQ14mo, LSQ13bdq, PTF12dam, CSS121015:004244+132827, PS1-11ap, SCP 06F6, PTF09cnd, PS1-10bj, and iPTF13ajg. This is due to the fact that for the purposes of our study, we decided to include only events with real detections shortly after the explosion and a good coverage of the LC in order to tightly constrain their LC shape parameters. N15, on the other hand, opted to use polynomial extrapolation to earlier times for some of the SLSNe in their sample in order to obtain estimates for tr_1

³ <https://github.com/mnicholl/superbol>

Table 1
The SLSN LC Sample Used for This Work

SLSN	Reference	z	Filters ^a	tr_1	td_1	s_1	tr_2	td_2	s_2	tr_3	td_3	s_3
<i>SLSN-I</i>												
PTF09cnd	Quimby et al. (2011)	0.258	<i>UBgRi</i>	29.5	56.3	0.52	18.9	26.9	0.7	10.6	12.9	0.82
SN2011kg	Inserra et al. (2013)	0.192	<i>UBgrizJ</i>	20.5	30.0	0.68	12.5	15.9	0.79	6.9	7.9	0.88
SN2010md	Inserra et al. (2013)	0.098	<i>UBgriz</i>	30.4	31.9	0.95	16.1	16.6	0.97	8.4	8.4	1.0
SN2213-1745	Cooke et al. (2012)	2.046	<i>g'r'i'</i>	10.4	25.5	0.41	6.7	8.6	0.78	3.7	4.3	0.87
PTF09atu	Quimby et al. (2011)	0.501	<i>gRi</i>	48.8	50.9	0.96	29.9	30.2	0.99	16.4	16.0	1.02
iPTF13ajg	Vreeswijk et al. (2014)	0.740	<i>uBgR_ziz</i>	21.9	28.8	0.76	14.3	16.4	0.87	8.0	8.6	0.93
PS1-10pm	McCrum et al. (2015)	1.206	<i>griz</i>	27.9	25.4	1.1	14.9	15.0	0.99	7.9	7.9	1.0
PS1-14bj	Lunnan et al. (2016)	0.522	<i>grizJ</i>	81.6	138.2	0.59	49.2	64.9	0.76	27.2	32.4	0.84
SN2013dg	Nicholl et al. (2014)	0.265	<i>griz</i>	15.6	29.7	0.52	10.4	14.0	0.74	5.9	6.8	0.87
iPTF13ehe	Yan et al. (2015, 2017)	0.343	<i>gri</i>	53.4	62.1	0.86	32.2	35.4	0.91	18.1	18.1	1.0
LSQ14mo	Leloudas et al. (2015)	0.253	<i>Ugri</i>	16.2	25.3	0.64	10.9	14.0	0.78	6.2	7.1	0.87
PS1-10bzj	Lunnan et al. (2013)	0.650	<i>griz</i>	14.6	22.5	0.65	10.3	13.8	0.75	6.1	7.2	0.84
DES14X3taz	Smith et al. (2016)	0.608	<i>griz</i>	31.9	41.8	0.76	19.9	23.0	0.87	11.0	11.7	0.94
LSQ14bdq	Nicholl et al. (2015b)	0.345	<i>griz</i>	54.6	90.2	0.61	37.1	48.8	0.76	21.7	24.4	0.89
SNLS 07D2bv	Howell et al. (2013)	1.500	<i>griz</i>	18.9	17.7	1.07	12.5	12.8	0.98	7.1	7.0	1.01
SNLS 06D4eu	Howell et al. (2013)	1.588	<i>griz</i>	15.0	17.6	0.85	9.4	10.6	0.89	5.3	5.7	0.92
PTF12dam	De Cia et al. (2018)	0.107	<i>UBgVrizJHK</i>	46.2	75.0	0.62	28.8	37.5	0.77	16.6	18.3	0.91
SN2011ke	De Cia et al. (2018)	0.143	<i>UBgVriz</i>	22.1	26.6	0.83	12.3	13.8	0.97	6.8	7.0	0.97
PTF12gty	De Cia et al. (2018)	0.177	<i>gri</i>	46.4	65.9	0.70	24.9	27.0	0.92	14.0	15.2	0.92
PS1-11ap	Lunnan et al. (2018a)	0.524	<i>grizy</i>	26.7	52.5	0.51	18.5	26.3	0.71	11.0	12.9	0.85
SCP 06F6	Barbary et al. (2009)	1.189	<i>iz</i>	31.8	32.7	0.97	19.5	19.5	1.0	10.6	10.4	1.02
<i>SLSN-II</i>												
SN2006gy	Smith et al. (2007)	0.019	<i>BVR</i>	41.0	54.3	0.76	24.4	27.8	0.88	13.3	14.1	0.94
CSS121015:004244+132827	Benetti et al. (2014)	0.287	<i>UBVRGI</i>	20.3	30.9	0.66	12.5	15.2	0.82	7.0	7.6	0.92
SN2016jhn	Moriya et al. (2018c)	1.965	<i>GI2zY</i>	12.4	27.0	0.46	10.3	20.7	0.5	6.3	10.6	0.6
SDSSII SN2538	Sako et al. (2018)	0.530	<i>u'g'r'i'z'</i>	31.6	37.8	0.84	19.0	19.2	0.99	10.0	10.0	1.0

Notes. The SLSN LC data were collected from the Open Supernova Catalog (Guillochon et al. 2017) database. All timescales are in units of days.

^a This column lists the filters used to compile the pseudo-bolometric LC of each SLSN in our sample.

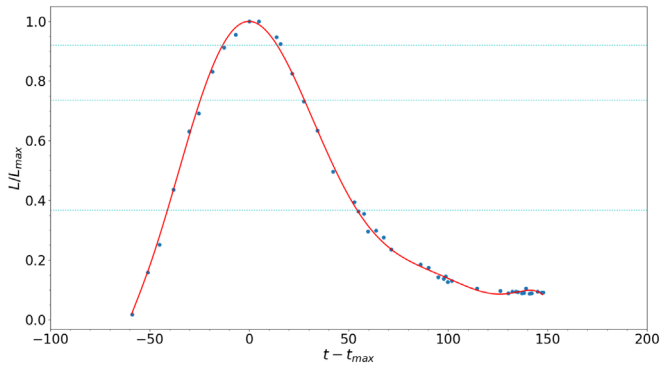


Figure 1. Polynomial fit (red curve) to the observed scaled pseudo-bolometric LC of Type II SN2006gy (blue circles). An eighth-degree polynomial is used for the fit. The primary, secondary, and tertiary luminosity thresholds are shown as horizontal light blue lines.

and td_1 . For objects where this extrapolation is done only by a few days, this may not be a bad approximation; however, the LCs for cases like SN2007bi (Gal-Yam et al. 2009), SN2005ap (Quimby et al. 2007), and PS1-10ky (Chomiuk et al. 2011), tr_1 is poorly constrained using this method.

For the 11 events that are common between our sample and that of N15, we calculate the mean value of tr_1 to be 27.2 days versus 25.7 days in their case, and the mean value of td_1 to be 42.8 days compared to 51.6 days in their case. Although our results are consistent in terms of tr_1 , the discrepancy observed in td_1 could be due to a variety of reasons including different

combinations of filters used to calculate the rest-frame pseudo-bolometric LC of each event. In our work, we have used all available filters with more than two data points for each event to construct LCs using SuperBol as described earlier. We caution that more accurate consideration for near-IR and IR fluxes may lead to the flattening of the true bolometric LC at late times and therefore longer primary decline timescales.

We note that comparing the mean tr_1 and td_1 values of our entire sample ($tr_1 = 30.8$ days, $td_1 = 43.9$ days from Table 2) against those of the full SLSN sample of N15 (their Table 3; $tr_1 = 22.9$ days, $td_1 = 46.4$ days), the agreement is somewhat better, within uncertainties. We also derive a linear fit for the observed tr_1 and td_1 values of the form:

$$td_1 = \gamma_0 + \gamma_1 \times tr_1, \quad (1)$$

where $\gamma_0 = -1.962$ and $\gamma_1 = 1.489$ (see also Figure 5). In contrast, N15 derived a steeper correlation for their “gold” SLSN sample with $\gamma_{0,N15} = -0.10$ and $\gamma_{1,N15} = 1.96$.

An investigation of Table 1 reveals yet another interesting property of our observed SLSN sample: five SLSN-I events SN2010md, PTF09atu, PS1-10pm, SNLS 07D2bv, and SCP 06F6) or, equivalently, 23.81% of the entire SLSN-I sample have fully symmetric LCs around peak luminosity, following the criterion we established earlier for full LC symmetry ($0.9 < s_{1,2,3} < 1.1$). This can be said for more certainty for SN2010md and PTF09atu (with redshifts 0.098 and 0.5 accordingly) compared to the other three events with large redshifts (>1), because in this case the observed band

Table 2
Main Statistical Properties of the Observed SLSN LC Sample Used in This Work

Parameter	μ	M	σ	max	min	μ	M	σ	max	min
SLSN-I					SLSN-II					
tr_1	31.6	27.9	17.3	81.6	10.4	26.3	25.9	10.9	41.0	12.4
td_1	45.1	31.9	28.5	138.2	17.6	37.5	34.3	10.4	54.3	27.0
s_1	0.74	0.70	0.19	1.10	0.41	0.68	0.71	0.14	0.84	0.46
tr_2	19.5	16.1	10.5	49.2	6.7	16.6	15.8	5.6	24.4	10.3
td_2	23.4	16.6	13.6	64.9	8.6	20.7	19.9	4.5	27.8	15.3
s_2	0.85	0.87	0.10	1.00	0.70	0.80	0.85	0.18	0.99	0.50
tr_3	10.9	8.4	5.9	27.2	3.7	9.1	8.5	2.8	13.3	6.2
td_3	11.9	8.6	6.7	32.4	4.3	10.6	10.3	2.3	14.1	7.6
s_3	0.93	0.92	0.06	1.02	0.82	0.86	0.93	0.16	1.00	0.60

Note. The parameters μ , M , σ , max, and min correspond to the values of the mean, median, standard deviation, maximum, and minimum of the sample accordingly. All timescales are in units of days.

correspond to near-UV fluxes in the rest frame. Bias toward UV fluxes may correspond to faster post-maximum decline rate and thus steeper, more symmetric LCs. Nevertheless, we have attempted to account for this effect by making use of approximate extrapolations to the IR flux by using the techniques available in SuperBol.

The upper left panel of Figure 4 shows two examples of SLSNe with “fully symmetric” LCs. Given that symmetric LCs are present in about a quarter of our SLSN-I sample, a considerable fraction of LC models corresponding to the proposed power input mechanisms must be able to reproduce this observation. This raises the question of whether LC symmetry is a property shared among all the proposed power input mechanisms for different combinations of model parameters or is uniquely tied to one power input mechanism. In the latter case, we can use photometry alone to characterize the nature of SLSNe.

Lastly, another LC shape property that will be interesting to constrain with future, high-cadence photometric follow-up of SLSNe would be the convexity (second derivative) of the bolometric LC during the rise to peak luminosity (Wheeler et al. 2017). Given the low temporal resolution of the observed LC in our sample, we opt to not provide estimates of the percentages of concave-up and concave-down LCs, yet we briefly discuss the predictions for these parameters coming from semianalytical models in the following section.

3. SLSN Power Input Models

A number of models have been proposed to explain both the unprecedented peak luminosities but, more importantly, the striking diversity in the observed properties of SLSNe, both photometrically (LC timescales and shapes) and spectroscopically (SLSN-I versus SLSN-II class events). The three most commonly cited SLSN power input mechanisms are the radioactive decay of several masses of ^{56}Ni produced in a full-fledged pair-instability supernova explosion (PISN; Gal-Yam et al. 2009; Chatzopoulos & Wheeler 2012b; Chatzopoulos et al. 2015), the magnetorotational energy release from the spindown of a newly born magnetar following a core-collapse SN (Kasen & Bildsten 2010; Woosley 2010), and the interaction between SN ejecta and massive, dense circumstellar shells ejected by the progenitor star prior to the explosion (Smith & McCray 2007; Smith et al. 2008; Chatzopoulos et al. 2016; Wheeler et al. 2017).

We have decided to leave the PISN model outside of our analysis because of several reasons that make it unsuitable for contemporary SLSNe. First, given that the known hosts of SLSNe have metallicities $Z > 0.1$ (Lunnan et al. 2013, 2014), very massive stars that formed in these environments are likely to suffer strong radiatively driven mass loss, preventing them from forming the massive carbon–oxygen cores ($\gtrsim 40\text{--}60 M_{\odot}$, depending on the zero age main sequence rotation rate; Chatzopoulos & Wheeler 2012b) required to encounter pair instability (Langer et al. 2007). Second, the majority of PISN models do not yield superluminous LCs. Yet even many of the PISN superluminous LCs require total SN ejecta masses that are comparable to—or smaller than in some cases—to the predicted ^{56}Ni mass needed to explain the high peak luminosity (Chatzopoulos et al. 2013). Finally, while radiation transport models of PISNe can reproduce superluminous LCs and provide good fits to the LCs of some SLSNe (Gal-Yam et al. 2009; Gilmer et al. 2017), the model spectra are too red compared to the observed SLSN spectra at contemporaneous epochs (Dessart et al. 2013; Chatzopoulos et al. 2015). Full-fledged PISNe may, however, still be at play in lower metallicity environments and massive, Population III primordial stars. For an alternative perspective on the viability of low-redshift full-fledged PISNe, we refer to Kozyreva et al. (2014).

We add that a model that is recently gaining popularity is energy input by fallback accretion into a newly formed black hole following core collapse (Dexter & Kasen 2013). One caveat of this model is that unrealistically large accretion masses are needed in order to fit the observed LCs of SLSNe given a fiducial choice for the energy conversion efficiency for the most cases (Moriya et al. 2018a). While the fallback accretion model is a very interesting suggestion that may be relevant to a small fraction of SLSNe, we opt to exclude it from our model LC shape analysis at least until it is further investigated in the literature. This leaves us with two main channels to power SLSNe often discussed today, the magnetar spindown and the circumstellar interaction model. Hereafter, we refer to the magnetar spindown model as “MAG” and to the SN ejecta–circumstellar matter interaction model as “CSM.”

For both the MAG and the CSM models, we adopt the semianalytic formalism presented in Chatzopoulos et al. (2012, 2013, hereafter C12, C13) and based on the seminal works of Arnett (1980, 1982) on modeling the LCs of SNe Ia and SNe II. While these models invoke many simplifying assumptions (centrally concentrated input source—in terms of energy

density, homologous expansion of the SN ejecta, and constant Thompson-scattering opacity for the SN ejecta, to name a few), they remain a powerful tool to study the LC shapes of SNe, assuming different power inputs because of their ability to provide reasonable estimates of the associated physical parameters when fit to observed data. In addition, these semianalytic models are numerically inexpensive to compute, allowing us to compute large grids of LC models throughout the associated multidimensional parameter space. As such, they remain a popular SN LC modeling tool with a few codes that have been made publicly available to compute them, such as TigerFit (Wheeler et al. 2017) and MOSFiT (Guillochon et al. 2018). We caution, however, that comparisons against rigorous, numerical radiation transport models have shown that semianalytic SLSN LC models have their limitations, especially in regimes where the SN expansion is not homologous (for example, due to circumstellar interaction) and due to the assumption of constant opacity in the SN ejecta and constant diffusion timescale (Moriya et al. 2013b; Khatami & Kasen 2018). For this reason, we include some analysis of the LC shape properties of numerically computed SLSN LCs that are available in the literature for both the MAG and the CSM models.

3.1. The SN Ejecta–Circumstellar Matter Interaction Model (CSM)

Massive stars can suffer significant mass-loss episodes, especially during the late stages of their evolution, due to a variety of mechanisms: super-Eddington strong winds during a luminous blue variable (LBV) stage similar to η Carina (Smith & McCray 2007; Smith et al. 2011; Jiang et al. 2018; Smith et al. 2018), gravity-wave-driven mass loss excited during vigorous shell Si and O shell burning (Quataert & Shiode 2012; Shiode & Quataert 2014; Fuller 2017), binary interactions (Woosley et al. 1994) or a softer version of PISN that does not lead to the complete disruption of the progenitor star (pulsational pair-instability supernova or PPISN; Woosley et al. 2007; Chatzopoulos & Wheeler 2012a; Woosley 2017). PPISNe originate from progenitors less massive than those from which full-fledged PISNe originate and can thus occur in the nearby universe, offering a channel to produce a sequence of SLSN-like transients originating from the same progenitor as successively ejected shells can collide with each other before the final CCSN takes place (Chatzopoulos et al. 2016; Woosley 2017; Lunnan et al. 2018b).

As a result, both observational evidence and theoretical modeling suggest that the environments around massive stars can be very complicated with diverse geometries (circumstellar (CS) spherical or bipolar shells, disks, or clumps) and, in some cases, very dense and at the right distance from the progenitor star that a violent interaction will be imminent following the SN explosion. This SN ejecta–circumstellar matter interaction (CSI) leads to the formation of forward and reverse shocks and the efficient conversion of kinetic energy into luminosity (Chevalier & Fransson 1994; Chevalier & Irwin 2011) that can produce superluminous transients with immense diversity in their LC shapes and maybe even spectra (Moriya & Tominaga 2012; Moriya et al. 2013a; Dessart et al. 2016; Kleiser et al. 2018).

C12 combined the self-similar CSI solutions presented by Chevalier & Fransson (1994) with the Arnett (1980, 1982) LC modeling formalism to compute approximate, semianalytical CSM models that were then successfully fit to the LCs of

several SLSN-I and SLSN-II events in C13. Given an SN explosion energy (E_{SN}), SN ejecta mass (M_{ej}), the index of the outer (power-law) density profile of the SN ejecta (n , related to the progenitor radius), the distance of the CS shell (R_{CS}), the mass of the CS shell M_{CS} , the (power-law) density profile of the CS shell (s), and the progenitor star mass-loss rate (\dot{M}), a model semianalytic CSM LC can be computed. The energy input originates from the efficient conversion of the kinetic energy of both the forward and reverse shocks to luminosity. As such, forward shock energy input is terminated when it breaks out to the optically thin CS while reverse shock input is terminated once it sweeps up the bulk of the SN ejecta. This is a property unique to the CSM model and not present in other, continuous heating sources such as radioactive decay of ^{56}Ni and magnetar spindown input: during CSI energy input terminates abruptly, thus affecting the shape of the LC in a way that can yield a faster decline in luminosity at late times.

While the CSM model can naturally explain the observed diversity of SLSN LCs and is consistent with the observation of narrow emission lines in the spectra of SLSN-II events of IIn class, it has been challenged as a viable explanation for SLSNe-I, due to the lack of spectroscopic signatures associated with interaction (Inserra et al. 2013, N15). There is, however, a “hybrid” class of SLSNe that transitions from SLSN-I to SLSN-II at late times, indicating possible interaction with H-poor material early on before the SN ejecta reach the ejected H envelope and interact with it, producing Balmer emission lines (Yan et al. 2015). Another concern for the CSM model is the necessity to include many parameters in the model that can lead to overfitting observed data and to parameter degeneracy issues (Moriya et al. 2013b). Detailed radiation hydrodynamics and radiation transport modeling of the CSI process across the relevant parameter space, including in cases of H-poor CSI, are still needed in order to resolve whether SLSNe-I can be powered by this mechanism.

3.2. The Magnetar Spindown Model (MAG)

The spindown of a newly born magnetar following CCSN can release magnetorotational energy that, if efficiently thermalized in the expanding SN ejecta, can produce a superluminous display (Kasen & Bildsten 2010; Woosley 2010). Given a dipole magnetic field for the magnetar, an initial rotation period of P_{mag} in units of 1 ms and an initial magnetar magnetic field $B_{14,\text{mag}}$ in units of 10^{14} G, the associated SN LC can be computed by making use of Equation (13) of C12. This model LC can also provide estimates for the SN ejecta mass, M_{ej} , that is controlled by the diffusion timescale (Equation (10) of C12).

Numerical radiation transport simulations of SNe powered by magnetars have yielded additional insights into the efficiency of this model in powering SLSNe, primarily of the hydrogen-poor (SLSN-I) type (Dessart et al. 2012; Metzger et al. 2015; Dessart 2018; Dessart & Audit 2018). Some observational evidence linking the host properties of SLSNe-I to those of LGRBs (Lunnan et al. 2014) and the discovery of double-peaked SLSN LCs, a feature that can be produced by magnetar-driven shock breakout (Nicholl et al. 2015b; Kasen et al. 2016), seem to strongly suggest that most, if not all, SLSNe-I are powered by this mechanism. This is strengthened by the suggestion that a lot of SLSN LCs can be successfully fit by a semianalytical MAG LC model (Nicholl et al. 2017; De Cia et al. 2018). There is, however, ongoing discussion on

whether the MAG model is always efficient in thermalizing the magnetar luminosity in the SN ejecta or even allowing for the efficient conversion of the magnetar energy to radiated luminosity (Bucciantini et al. 2006), instead of kinetic energy for the inner ejecta (Wang et al. 2016). Recent 2D simulations of magnetar-powered SNe appear to enhance these concerns (Chen et al. 2016, 2017).

3.3. Grids of Models with the TigerFit Code

We have adapted the TigerFit code (Chatzopoulos et al. 2016; Wheeler et al. 2017) to run grids of CSM and MAG models throughout a large parameter space in order to systematically study the statistical LC shape properties and determine their association with the observed SLSN sample presented in Section 2.

For the CSM model, we consider cases with H-poor opacity (CSM-I; $\kappa = 0.2 \text{ cm}^2 \text{ g}^{-1}$) and H-rich opacity ($\kappa = 0.4 \text{ cm}^2 \text{ g}^{-1}$) and run two sets of grids: (a) CSM-I κ /CSM-II κ models, where the parameter grid is identical, and (b) CSM-I/CSM-II models, where the parameter grid is constrained in each case, motivated by assumptions about the nature of the progenitor stars in SNe I versus SNe II, respectively, that are further discussed later in this section. For case (a), the ranges used for each parameter are as follows:

1. $E_{\text{SN},51} \in [1.0, 1.2, 1.5, 2.0]$, where $E_{\text{SN}} = E_{\text{SN},51} \times 10^{51} \text{ erg}$,
2. $M_{\text{ej}} \in [5, 8, 10, 15, 20, 25, 30, 40]$, where M_{ej} is in units of M_{\odot} ,
3. $n \in [7, 8, 9, 10, 11, 12]$,
4. $R_{\text{CS},15} \in [10^{-5}, 10^{-4}, 10^{-3}, 10^{-2}, 10^{-1}]$, where $R_{\text{CS}} = R_{\text{CS},15} \times 10^{15} \text{ cm}$,
5. $M_{\text{CS}} \in [0.1, 0.2, 0.5, 1.0, 2.0, 5.0, 8.0]$, where M_{CS} is in units of M_{\odot} ,
6. $\dot{M} \in [0.001, 0.01, 0.05, 0.1, 0.2, 0.5, 1]$, where \dot{M} is in units of $M_{\odot} \text{ yr}^{-1}$.

For case (b) and the CSM-I subset, the ranges used are

1. $E_{\text{SN},51} \in [1, 1.2, 1.5, 1.75, 2]$,
2. $M_{\text{ej}} \in [5, 8, 10, 12, 15, 20, 25, 30]$,
3. $n \in [7, 8, 9]$,
4. $R_{\text{CS},15} \in [10^{-5}, 10^{-4}, 5 \times 10^{-4}, 10^{-3}, 5 \times 10^{-3}, 10^{-2}]$,
5. $M_{\text{CS}} \in [0.1, 0.2, 0.5, 0.7, 1.0, 2.0, 5.0]$,
6. $\dot{M} \in [10^{-5}, 10^{-4}, 10^{-3}, 0.01, 0.1, 0.2, 0.5, 1.0, 2.0]$,

and accordingly for the CSM-II subset,

1. $E_{\text{SN},51} \in [1, 1.2, 1.5, 1.75, 2]$,
2. $M_{\text{ej}} \in [12, 15, 20, 25, 30, 40, 50, 60]$,
3. $n \in [10, 11, 12]$,
4. $R_{\text{CS},15} \in [0.01, 0.05, 0.08, 0.10, 0.20, 0.30]$,
5. $M_{\text{CS}} \in [0.5, 1.0, 2.0, 5.0, 8.0, 10.0, 15.0]$,
6. $\dot{M} \in [10^{-5}, 10^{-4}, 10^{-3}, 0.01, 0.1, 0.2, 0.5, 1.0, 2.0]$.

For all CSM models, we are focusing on the $s = 0$ cases implying a fiducial, constant-density circumstellar shell. While the $s = 2$ case is of interest because it implies a radiatively driven wind structure that is common around red supergiant stars (RSGs), we omit it in this work because it is inconsistent with episodic mass loss, which is more likely to be the case for luminous SNe. Also, for the vast majority of cases where the $s = 2$ choice yields luminous LCs, other parameters obtain unrealistic values (for example, M_{CS} values in excess of $\sim 100 M_{\odot}$ are commonly found; C13). As a result, a total of

47,040 models were generated for the CSM-I κ /CSM-II κ cases and 45,360 models for the CSM-I/CSM-II cases.

Our motivation for adopting different parameter ranges for the CSM-I and CSM-II models stems from several factors. First, larger M_{CS} values are possible in the CSM-II case as suggested by spectroscopic observations of SLSNe-II of Type IIn (Smith et al. 2010), where stronger mass loss pertains, due to LBV-type or PPISN processes (Smith 2014). That, in turn, also implies larger progenitor masses (and therefore M_{ej}) for CSM-II, as in the case for regular luminosity SNe, where LC fits imply larger M_{ej} , and therefore larger diffusion timescales, for Type II events than for Type I SNe. Finally, lower values of n are more typical of compact, blue supergiant (BSG) progenitors with radiative envelopes while higher values imply extended, RSG-type convective envelopes that are more appropriate for SLSNe-II (Chevalier & Fransson 2003). In summary, the CSM-II parameters are associated with RSG-type progenitors with extended H-rich envelopes while the CSM-I parameters are associated with more compact, BSG-type stars.

We caution that one potential issue with our choices for model parameter grids is that there are no good observational constraints yet on what the shape of the distribution of SN ejecta and circumstellar shell masses should be, so using these models in a clustering analysis (Section 4) might be misleading as it can create dense clusters of models that might actually be very sparsely populated in nature, or conversely, an underdensity of points in regions where more MAG or CSM SNe might lie in reality. Our grid selection for M_{CS} is largely driven by published observations of nebular shells around massive, LBV-type stars indicating $M_{\text{CS}} \simeq 0.1\text{--}20 M_{\odot}$ (Smith & Owocki 2006; Groh et al. 2009; Gvaramadze et al. 2010; Wachter et al. 2010; Smith 2014). The ranges for M_{ej} are within typical ranges for stars massive enough to experience an SN, and in agreement with observations of SN progenitor stars in pre-explosion images and supernova remnants ($M_{\text{ej}} \simeq 8\text{--}25 M_{\odot}$; Smartt 2009; Morozova et al. 2018; Auchettl et al. 2019). Higher mass progenitors cannot be excluded given observations of stars as massive as $>150 M_{\odot}$ in the Milky Way galaxy (Crowther et al. 2010).

For the MAG model, we investigate a dense grid of models with $10^{12} < B_{\text{MAG}} < 10^{15} \text{ G}$ and $1.0 < P_{\text{MAG}} < 50 \text{ ms}$, where B_{MAG} and P_{MAG} are the magnetic field and the initial rotational period of the magnetar, respectively. We are also varying the diffusion timescale, t_{d} , that further controls the shape of MAG model LCs (Equation (13) of C12), in the range $3 < t_{\text{d}} < 100$ days. The grid resolution we use for these parameters results in a total of 46,656 MAG model LCs generated.

A large fraction of CSM and MAG models did not produce superluminous LCs, which we take to be those reaching $L_{\text{max}} = 10^{44} \text{ erg s}^{-1}$ or more (Gal-Yam 2012). These models are ignored from each of our CSM and MAG model samples for further analysis. In addition, we exclude model LCs that result in physically inconsistent parameters such as combinations of B_{MAG} and P_{MAG} values in the MAG model that are incompatible with the convective dynamo process in magnetars (Duncan & Thompson 1992) and in CSM models that yield M_{CS} that are too large compared to the associated M_{ej} values that represent a measure of the total progenitor mass.

As a result, our original CSM-I/CSM-II, CSM-I κ /CSM-II κ , and MAG model samples are each reduced into smaller subsamples of nearly equal size that are then used in our final LC shape parameter analysis. More specifically, a total of 306

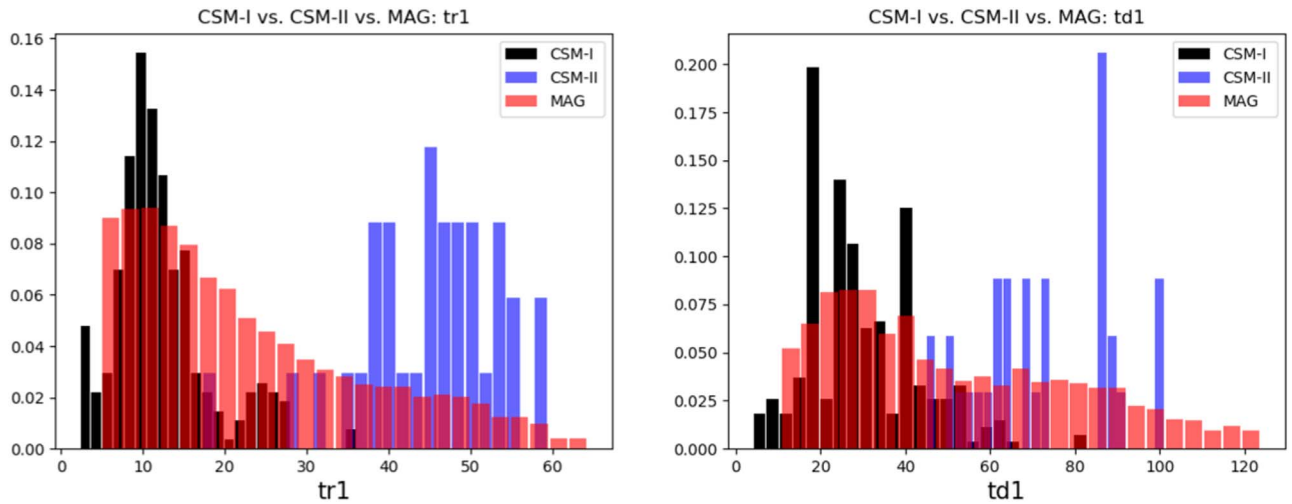


Figure 2. Distribution of primary rise (tr_1 ; left panel) and decline (td_1 ; right panel) timescales for the CSM-I (black bars), CSM-II (blue bars), and MAG (red bars) model samples.

Table 3
Main Statistical Properties of the CSM-I and CSM-II Model Samples Used in This Work

Parameter	μ	M	σ	max	min	μ	M	σ	max	min
CSM-I						CSM-II				
tr_1	12.2	11.0	5.9	36.1	2.3	45.1	46.6	8.8	59.5	17.3
td_1	29.7	28.6	13.2	82.8	4.0	72.6	69.5	16.1	101.1	44.9
s_1	0.43	0.41	0.15	0.87	0.13	0.64	0.61	0.13	1.00	0.37
tr_2	7.0	6.0	4.0	28.2	1.3	18.7	19.4	3.7	25.4	7.1
td_2	9.1	8.4	5.0	33.3	1.5	24.4	25.9	4.7	31.7	11.8
s_2	0.78	0.77	0.15	1.15	0.52	0.77	0.74	0.14	1.14	0.60
tr_3	2.9	2.2	2.6	18.9	0.5	6.1	6.1	1.2	8.3	2.5
td_3	3.1	2.4	3.1	24.4	0.5	7.0	7.2	1.4	10.2	3.0
s_3	0.92	0.93	0.11	1.10	0.73	0.88	0.85	0.10	1.09	0.73

CSM-I/CSM-II, 248 CSM-I κ /CSM-II κ , and 304 MAG superluminous LC models are used in this work. The statistical properties of the LC shape parameters of all models are summarized in Tables 3–5. Figures 2 and 3 show the distribution of a few LC shape parameters (tr_1 , td_1 , s_1 , s_2 , s_3) for the CSM-I/CSM-II and MAG model samples, and Figure 4 shows examples of some of the most symmetric LCs in these samples.

For comparison against our semianalytical LCs, we have also included a sample of numerical CSM and MAG LCs available in the literature. Table 6 lists the details of the numerical model LCs, and Table 7 summarizes the statistics of their shape parameters. Figure 5 is a scatter plot between tr_1 and td_1 for all samples in this work, including the numerical MAG and CSM models. A linear best fit to the observed SLSN-I and SLSN-II data is also shown (see Equation (1)). Although we chose to not use different symbols for the CSM models as presented in Figure 5, it is evident by inspecting Table 4 that CSM-II models occupy the upper right corner of this plot given their longer primary rise and decline timescales. A few SLSNe-I thus appear to be associated with the CSM-II data that were chosen based on assumptions for the progenitors of H-rich SLSNe. The situation is different when looking at the CSM-I κ /CSM-II κ distribution, however, where the parameter grids are identical and the only difference is due to different SN ejecta + CS shell opacity. In this case, the primary timescales

of the models are consistent. Very slowly evolving H-poor SLSNe may be hard to produce under the assumption of H-poor CSM interaction given the large, H-deficient CS shell mass needed to account for the long primary rise and decline timescales. Interaction with a H-poor CS shells of nonspherical geometry in combination with viewing-angle effects may be a way out of this apparent discrepancy (Kleiser et al. 2018). Accordingly, Figure 6 shows a 3D scatter plot for the primary, secondary, and tertiary LC symmetry parameter for all samples. The superluminous LCs recovered result in the following mean values for the parameters of each model:

1. CSM-I: $E_{SN,51} = 1.75$, $M_{ej} = 10 M_{\odot}$, $n = 8$, $R_{CS,15} = 0.006$, $M_{CS} = 1 M_{\odot}$ and $\dot{M} = 0.01 M_{\odot} \text{ yr}^{-1}$,
2. CSM-II: $E_{SN,51} = 2.00$, $M_{ej} = 13 M_{\odot}$, $n = 12$, $R_{CS,15} = 0.2$, $M_{CS} = 10 M_{\odot}$ and $\dot{M} = 0.01 M_{\odot} \text{ yr}^{-1}$,
3. CSM-I κ : $E_{SN,51} = 1.80$, $M_{ej} = 10 M_{\odot}$, $n = 9$, $R_{CS,15} = 0.08$, $M_{CS} = 2 M_{\odot}$ and $\dot{M} = 0.15 M_{\odot} \text{ yr}^{-1}$,
4. CSM-II κ : $E_{SN,51} = 2.00$, $M_{ej} = 7 M_{\odot}$, $n = 9$, $R_{CS,15} = 0.1$, $M_{CS} = 0.3 M_{\odot}$ and $\dot{M} = 0.3 M_{\odot} \text{ yr}^{-1}$,
5. MAG: $B_{MAG} = 1.4 \times 10^{13} \text{ G}$ and $P_{MAG} = 1.3 \text{ ms}$.

These parameters are within the range of semianalytical and numerical fits of the CSM and MAG models to observed SLSN LCs commonly found in the literature.

A careful examination of the computed LC shape parameter distributions for the CSM and MAG models reveals a lot of

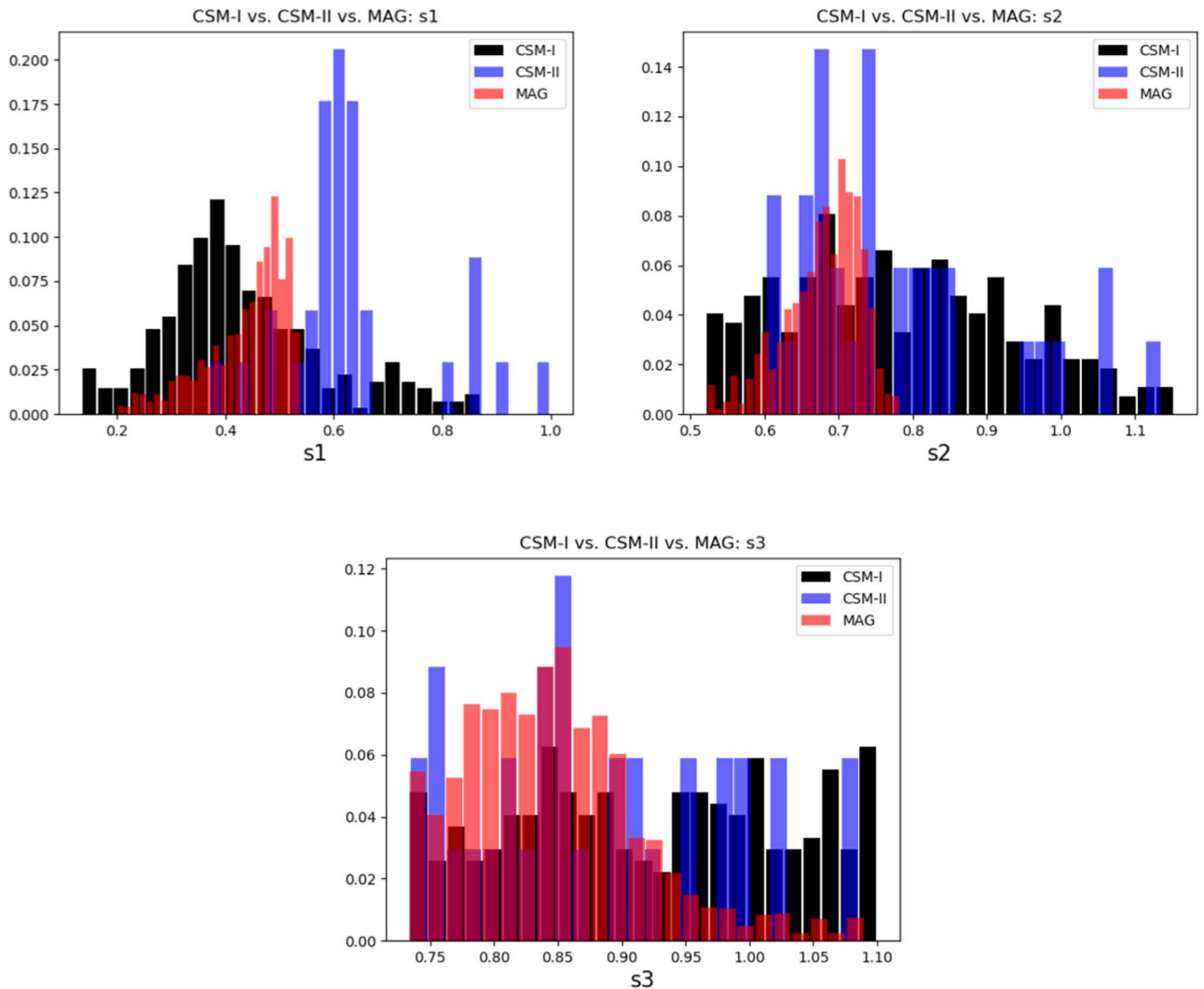


Figure 3. Same as Figure 2 but for primary (s_1 ; upper left panel), secondary (s_2 ; upper right panel), and tertiary (s_3 ; bottom panel) LC symmetry.

interesting insights. First, the primary rise and decline timescales appear to have a binary distribution for the CSM models with CSM-I models typically reaching shorter tr_1 and td_1 values than CSM-II models. This is both due to the physically motivated choices for the parameter grids discussed earlier, but also because of the opacity difference between H-rich and H-poor models. On the other hand, the MAG models show a more continuous and single-peaked distribution with typical values $tr_1 \simeq 5\text{--}15$ days and $td_1 \simeq 20\text{--}30$ days. In terms of LC symmetry, the majority of models do not appear to produce symmetric LCs around the primary luminosity threshold as $0.9 < s_1 < 1.1$ values are rarely recovered. In fact, CSM is the only set of models reaching s_1 values close to unity while MAG is unable to produce any models with symmetric LCs both in terms of s_1 and s_2 . Even the most symmetric MAG LCs in our sample appear to have this issue (Figure 4). This is an important issue for MAG models given that a significant fraction of observed SLSNe-I are symmetric around these luminosity thresholds (Section 2). This seems to be the case for numerically computed MAG LC models as well, with the most symmetric one being model RE0p4B3p5 (Dessart & Audit 2018) with $s_1 = 0.84$. Numerical CSM models tend to yield more rapidly evolving LCs than their semianalytical counterparts. The primary source of this

difference is the assumption of a constant diffusion timescale in the semianalytical CSM models (Moriya et al. 2013b; Khatami & Kasen 2018).

We explore the possibility that gamma-ray leakage produces faster declining MAG LCs, therefore enhancing symmetry, by adopting the same formalism employed in the case of LCs powered by the radioactive decay of ^{56}Ni (Sutherland & Wheeler 1984; Clocchiatti & Wheeler 1997; Valenti et al. 2008; Chatzopoulos et al. 2013). Using a fiducial SN ejecta gamma-ray opacity of $\kappa_\gamma = 0.03 \text{ cm}^2 \text{ g}^{-1}$ and the implied SN ejecta mass for the two most symmetric MAG models shown in the top right panel of Figure 4, we adjust the output luminosity as $L'(t) = L(t)(1 - \exp - At^{-2})$, where $At^{-2} = \kappa_\gamma \rho R$. The two most symmetric MAG models with high gamma-ray leakage are then plotted as dashed curves. Allowing for gamma-rays to escape can increase the decline rate of the LC at late times, leading to shorter td_1 and slightly higher s_1 values. The change, however, still falls short in producing symmetric MAG LCs because s_1 only increases by 14%–22% and the maximum value for $s_1 \lesssim 0.6$.

Second, the observed tight $tr_1\text{--}td_1$ correlation in SLSN LCs is reproduced by both CSM and MAG models. CSM models generally predict faster evolving LCs at late times than MAG models, consistent with the observations. This is mainly due to

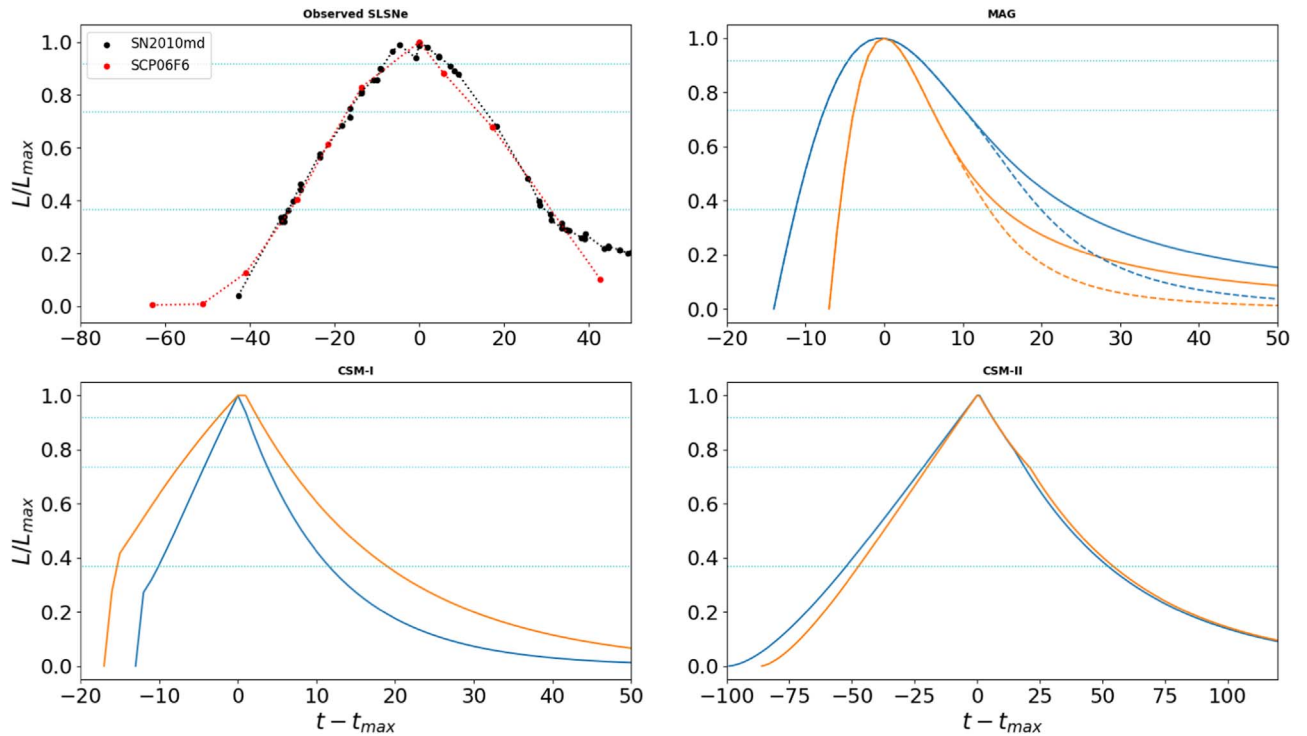


Figure 4. The most symmetric LCs of the observed SLSN sample (upper left panel), the MAG model sample (upper right panel), the CSM-I model sample (lower left panel), and the CSM-II model sample (lower right panel). The light blue dashed lines indicate the primary, secondary, and tertiary luminosity thresholds used to determine symmetry around peak luminosity (see Section 2.1). It can be seen that even the most symmetric MAG model LCs are still quite asymmetric at the primary luminosity threshold. This holds even under the assumption of strong γ -ray leakage (marked by dashed curves for each MAG model).

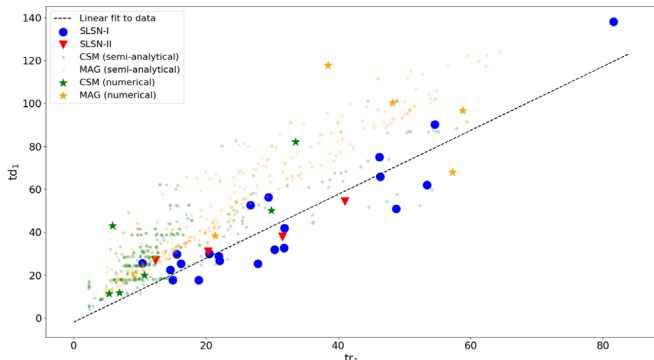


Figure 5. Distribution of tr_1 and td_1 for the semianalytical MAG (orange circles) and CSM (green circles) models compared to the observed SLSN-I (blue circles) and SLSN-II (red triangles) sample. The green and orange star symbols correspond to published numerical LC models (see 3). The dashed line represents a linear fit to the observed data.

the continuous power input in the MAG model that sustains a flatter LC at late times while in the CSM model the energy input is terminated abruptly, leading to rapid decline after peak luminosity (C12). An example of an SLSN with a very flat late-time LC is SN2015bn (Nicholl et al. 2018), indicating that this may be a good candidate for the MAG model. The observed LC symmetry parameter distributions (Figure 6) reveal a more distinct dichotomy between CSM and MAG models. MAG models fail to produce fully symmetric LCs and are clustered in a confined region of the 3D (s_1 , s_2 , and s_3) parameter space while CSM models are more scattered.

Finally, we estimate the fraction of CSM and MAG model SLSN LCs that have a concave-up shape during the rise to peak luminosity or, in other words, positive second derivative for

$t < t_{\max}$. An example of an observed SLSN with concave-up LC during the rise is SN 2017egm (Wheeler et al. 2017). Not a single MAG LCs is found to be concave-up during the rise. On the contrary, $\sim 20\%$ of CSM-I, $\sim 60\%$ of CSM-II, and $\sim 50\%$ of CSM-I κ /CSM-II κ models are found to have concave-up rise to peak luminosity. The implication is that the shape of the rising part of SLSN LCs may also be tied to the nature of the power input mechanism and, specifically, the functional form of the input luminosity. Continuous, monotonically declining power inputs like ^{50}Ni decay and magnetar spindown energy correspond to concave-down SLSN LCs, while truncated CSM shock luminosity input depends on the details of the SN ejecta and the circumstellar material density structure and can yield either concave-up or concave-down LCs during the early rising phase. This further enforces the need to obtain high-cadence photometric coverage of these events in future transient surveys.

4. k -means Clustering Analysis

k -means clustering is a powerful machine-learning algorithm used to categorize data via an iterative method (Lloyd 2006; MacQueen 1967). The standard version of this algorithm finds the locations and boundaries of “clusters” of data by repeatedly minimizing their Euclidean distances from cluster centroids. The user can either input the number of clusters, k , based on some assumption about the nature of the data or can use a density-based (“DBSCAN”) approach (Ester et al. 1996) to determine the optimal number of clusters. While k -means assumes clusters separated by straight-line boundaries, there exist clustering algorithms that relax that criterion. For the scope of this work to quantitatively characterize the LC shape properties of CSM and MAG models and determine if

Table 4
Main Statistical Properties of the CSM-I κ and CSM-II κ Model Samples Used in This Work

Parameter	μ	M	σ	max	min					
						μ	M	σ	max	min
CSM-I κ						CSM-II κ				
tr_1	15.1	12.6	8.3	50.3	2.5	11.9	11.5	3.5	22.1	3.3
td_1	32.2	30.5	16.0	83.2	3.3	25.3	22.9	10.7	49.7	5.0
s_1	0.50	0.48	0.18	1.03	0.16	0.52	0.48	0.16	0.86	0.26
tr_2	7.7	6.1	5.4	39.3	1.7	6.8	6.3	3.5	20.8	2.2
td_2	10.4	8.5	6.4	38.9	1.9	8.4	7.5	4.0	22.3	1.9
s_2	0.75	0.72	0.26	1.16	0.53	0.82	0.80	0.16	1.15	0.55
tr_3	3.1	2.3	3.4	26.3	0.6	2.6	2.1	2.4	15.2	0.9
td_3	3.6	2.5	4.2	32.5	0.6	2.9	2.5	2.9	18.6	1.0
s_3	0.90	0.89	0.10	1.10	0.74	0.90	0.89	0.10	1.09	0.74

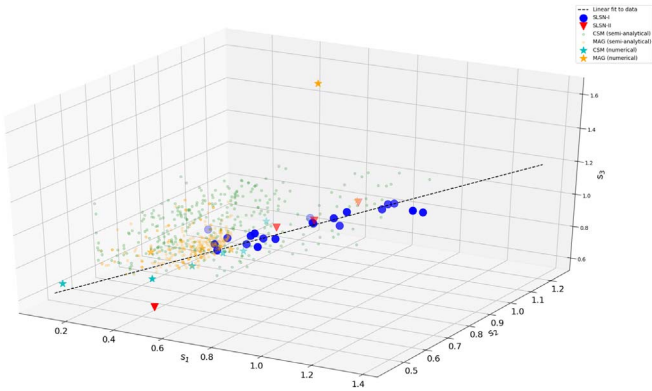


Figure 6. Same as Figure 5 but for s_1 , s_2 , and s_3 .

they occupy distinct areas of the parameter space, we employ k -means clustering analysis. More specifically, we use the Python scikit-learn (`sklearn`) package.

k -means clustering analysis is often used in astronomical applications aiming to classify astronomical objects in transient search projects (Wozniak et al. 2001; Zhang & Zhao 2004; Ordovás-Pascual & Sánchez Almeida 2014). Recently, it was utilized to classify the properties of SLSNe, based on both LC and spectroscopic features, showcasing the importance it holds for the future of the field. Nicholl et al. (2019) presented their work on k -means clustering analysis of SLSN nebular spectra properties. Inserra et al. (2018) illustrated how the method can be used to identify SLSNe-I and probe their observed diversity and identified two distinct groups: “fast” and “slow” SLSNe-I depending on the evolution of the LC and the implied spectroscopic velocities and SN ejecta velocity gradients.

In this work, we use k -means clustering to investigate if the SLSN LC shape properties implied by different power input models (MAG, CSM-I, and CSM-II) concentrate in distinct clusters. This may allow us to associate observed SLSNe with proposed power input mechanisms based only on the LC properties and thus provide a framework for SLSN characterization for future, big data transient searches like LSST. To do so, we focus on different combinations of k values and LC parameter space dimensionality (N_D). Given our prior knowledge that we are using LC shape parameter data from two categories (CSM, MAG) of models, we focus on two cases: $k = 2$ (CSM models of both type I and II and MAG) and $k = 3$ (distinct CSM-I, CSM-II, and MAG models). We also look at different values for N_D : 2D data sets focusing on the primary LC timescales (tr_1 , td_1), 3D data sets focusing on the LC

Table 5
Main Statistical Properties of the MAG Model Samples Used in This Work

Parameter	μ	M	σ	max	min
tr_1	22.8	18.7	14.3	64.4	4.9
td_1	50.8	43.3	28.4	123.9	10.7
s_1	0.44	0.46	0.08	0.54	0.20
tr_2	15.2	12.5	9.3	41.4	3.3
td_2	22.2	18.4	13.0	56.4	4.7
s_2	0.68	0.69	0.05	0.78	0.52
tr_3	8.8	7.2	5.3	23.5	1.9
td_3	10.5	8.7	6.4	27.1	2.06
s_3	0.85	0.84	0.07	1.09	0.73

symmetry parameters (s_1 , s_2 , s_3), 4D data sets focusing on the primary and secondary LC timescales (tr_1 , td_1 , tr_2 , td_2), and 6D data sets focusing on the primary, secondary, and tertiary LC timescales (tr_1 , td_1 , tr_2 , td_2 , tr_3 , td_3), thus covering all of the LC shape parameters defined in this work (given the six timescales, the symmetry parameters can be constrained). Although we only opted to perform clustering analysis for $k = 2, 3$ based on prior knowledge of the number of models used in the data sets, we also estimated the optimal number of clusters in all cases using the “elbow” method (Nche Tuma et al. 2009). This method is based on plotting the normalized squared error of clustering (E_N ; defined in the next paragraph) as a function of k and finding the value of k that corresponds to the sharpest gradient. This test confirmed that the optimal number of clusters for all data sets is $k = 2$.

While for the 2D and the 3D clustering we can provide visual representations of the clusters, that is impossible for the 4D and the 6D cases. For this reason, and in order to quantify the quality and accuracy of our clustering results, we use silhouette analysis (Rousseeuw 1987). Silhouette analysis yields a mean silhouette score, \bar{S} , and silhouette diagrams that visualize the sizes of the individual clusters and the S score distribution of the individual data within each cluster. Negative values of S correspond to falsely classified data while values closer to unity indicate stronger cluster association. Silhouette diagrams with clusters of comparable width and with S values above the mean are indicative of accurate clustering. An example silhouette diagram for the $k = 2, 3$ and $N_D = 4$ case we study in this work is shown in Figure 7. Figures 8 and 9 show the distribution of the computed clusters in the $N_D = 2$ and $N_D = 3$ cases for $k = 2$ with the SLSN-I/SLSN-II observations overplotted for comparison. The cluster centroids

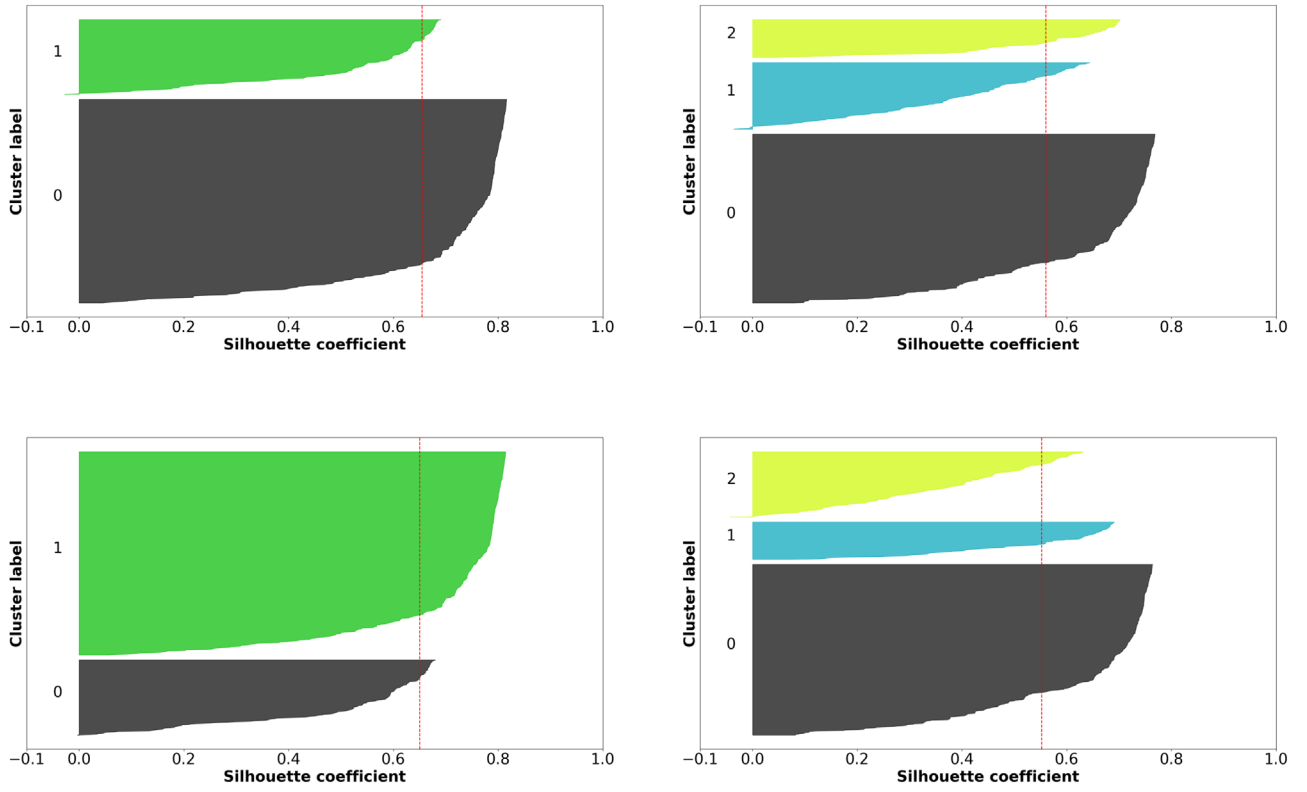


Figure 7. Silhouette analysis for the 4D (tr_1, td_1, tr_2, td_2 ; upper panels) and 6D ($tr_1, td_1, tr_2, td_2, tr_3, td_3$; lower panels) clustering done on the CSM-I/CSM-II/MAG data set. The $k = 2$ results are shown in the left column and the $k = 3$ results in the right column for both cases.

Table 6
The Numerical Models Sample

Model ID	Reference	Model Type	tr_1	td_1	s_1	tr_2	td_2	s_2	tr_3	td_3	s_3
B3	Dessart et al. (2016)	CSM-I	5.9	43.0	0.14	4.3	9.8	0.44	2.7	3.9	0.70
T130D-b	Woosley (2017)	CSM-I	6.9	11.9	0.59	4.3	5.8	0.75	2.3	2.9	0.80
D2	Moriya et al. (2013b)	CSM-II	29.9	50.1	0.60	19.0	22.7	0.84	10.5	11.3	0.93
F1	Moriya et al. (2013b)	CSM-II	33.5	82.0	0.41	23.3	43.1	0.54	13.7	18.8	0.73
R3	Dessart et al. (2016)	CSM-II	5.4	11.4	0.47	3.7	5.7	0.65	2.0	2.7	0.75
T20	Woosley (2017)	CSM-II	10.7	20.0	0.53	7.0	9.8	0.71	3.7	4.7	0.80
KB 1 (Black curve)	Kasen & Bildsten (2010)	MAG	21.4	38.5	0.56	13.7	18.8	0.73	7.7	9.4	0.82
KB 2 (Red curve)	Kasen & Bildsten (2010)	MAG	38.5	117.9	0.33	25.37	40.9	0.62	14.7	18.0	0.82
Model 2	Kasen et al. (2016)	MAG	48.2	100.3	0.48	33.6	49.3	0.68	20.2	24.1	0.84
RE3B1	Dessart & Audit (2018)	MAG	58.8	96.7	0.61	46.5	43.9	1.06	31.1	19.2	1.62
RE0p4B3p5	Dessart & Audit (2018)	MAG	57.3	68.0	0.84	34.8	35.6	0.97	19.0	18.6	1.02

Table 7
Main Statistical Properties of the Numerical Models

Parameter	μ	M	σ	max	min	μ	M	σ	max	min
CSM-I/CSM-II					MAG					
tr_1	15.4	8.8	33.5	5.4	11.7	44.8	48.2	58.8	22.4	13.8
td_1	36.4	31.5	82.1	11.4	25.2	84.3	96.7	117.9	38.5	28.0
s_1	0.46	0.50	0.60	0.14	0.16	0.56	0.56	0.84	0.33	0.17
tr_2	10.3	5.7	23.3	3.7	7.9	30.8	33.6	46.5	13.7	10.9
td_2	16.13	9.8	43.1	5.7	13.3	37.7	40.9	49.3	18.8	10.5
s_2	0.66	0.68	0.84	0.44	0.133	0.81	0.73	1.06	0.62	0.17
tr_3	5.8	3.2	13.7	2.7	4.6	18.5	19.0	31.1	7.7	7.7
td_3	7.4	4.3	18.8	2.7	5.9	17.9	18.6	24.1	9.4	4.8
s_3	0.79	0.78	0.93	0.70	0.07	1.02	0.84	1.62	0.82	0.31

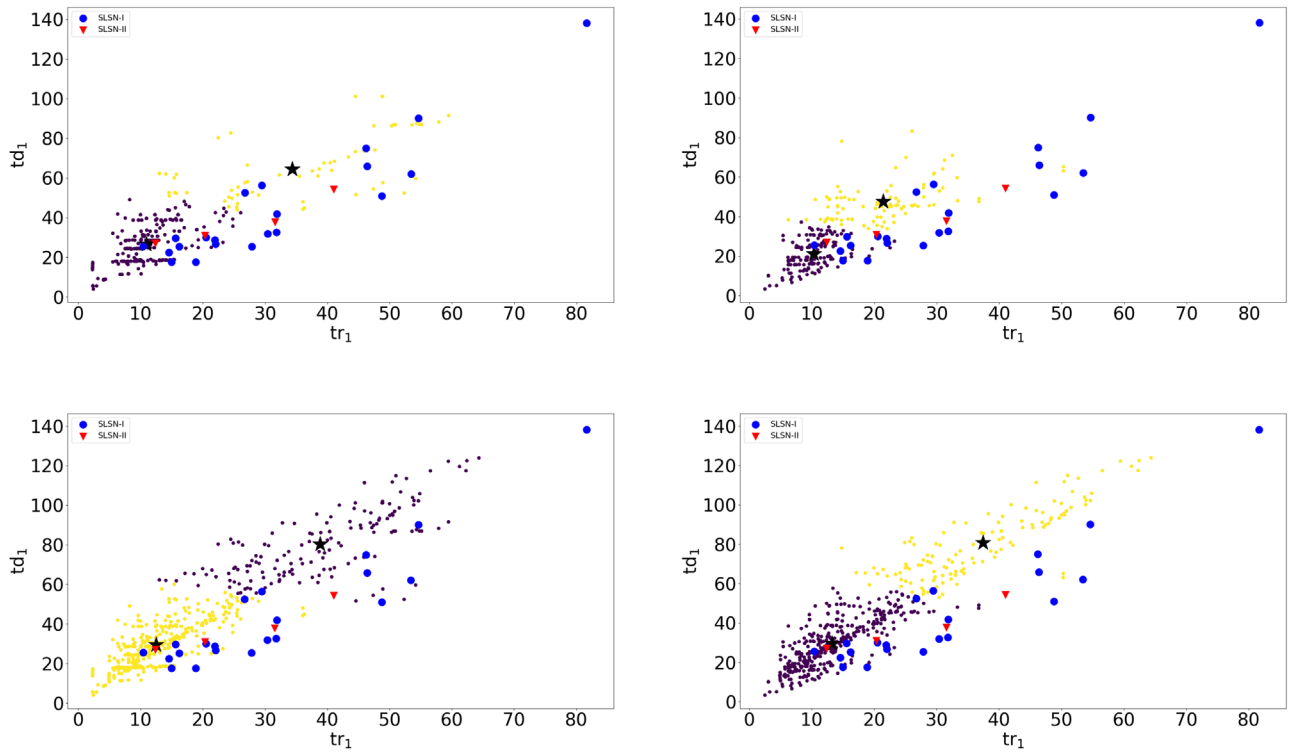


Figure 8. Clustering ($k = 2$) for the 2D CSM-I/CSM-II data set (upper left panel), the 2D CSM-I κ /CSM-II κ data set (upper right panel), the 2D CSM-I/CSM-II/MAG data set (lower left panel), and the 2D CSM-I κ /CSM-II κ /MAG data set (lower right panel). In each panel, the star symbols correspond to the cluster centroids, the blue circles to the observed SLSN-I sample, and the red triangles to the observed SLSN-II sample. For the 2D (tr_1, td_1) case, k -means clustering is unable to find clusters that significantly overlap with the MAG and CSM models (see Section 4).

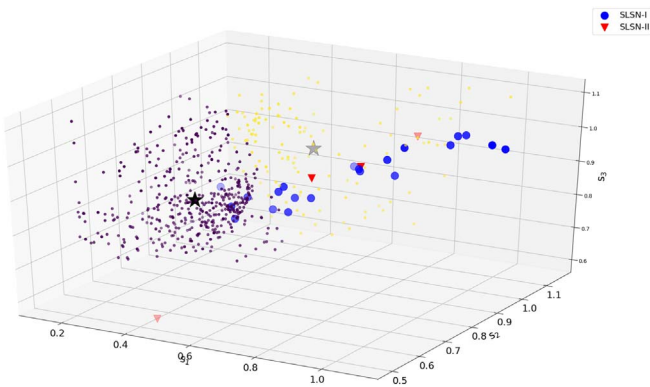


Figure 9. Same as in Figure 8 but for the 3D (s_1, s_2, s_3) CSM-I/CSM-II/MAG data set. The computed clusters associate with the underlying model categories better than in the 2D case (see Section 4).

are also marked with black star symbols. Table 8 presents the results of clustering analysis for each k - N_D combination that we investigated, including the normalized classification error (E_N ; the square-root of the sum of squared distances of samples to their closest cluster center divided by the cluster size) and \hat{S} , as well as the computed cluster compositions (percentage of CSM-I/CSM-II and MAG models within each cluster) and observed SLSN-I/SLSN-II cluster associations.

5. Results

5.1. $N_D = 2$

Our clustering analysis on the primary LC timescales (tr_1, td_1) reveals a clear dichotomy between H-rich and H-poor CSM

models in the CSM-I/CSM-II case where the first cluster (C_0) is composed by CSM-I (and, respectively, CSM-I κ) models by almost 100%. The observed SLSN-I and SLSN-II sample is not clearly associated with either cluster in the CSM-I/CSM-II case. For all combinations of model data sets and values of k , we find the $k = 2$ choice to correspond to more accurate clustering (higher \bar{S} scores). This is indicative that the value $k = 2$ may be optimal in distinguishing between CSM-type models of either type against MAG models. The CSM-I/CSM-II/MAG, $k = 2$ case has the highest \bar{S} score and yields the first cluster (C_0) dominated by MAG models ($\sim 76\%$ of the cluster data) and the second cluster (C_1) dominated by CSM-I/CSM-II models ($\sim 60\%$ of the cluster data). Nearly $\sim 75\%$ of observed SLSNe-I/SLSNe-II are associated with C_1 implying that, practically, both CSM- and MAG-type models can reproduce SLSN LCs in terms of the primary LC timescales. As such, the $N_D = 2$ case does not represent a robust way to distinguish between SLSNe powered by either the CSM or the MAG mechanism.

5.2. $N_D = 3$

In this case, we explore clustering for the three main LC symmetry parameters as defined in Section 2.1. As can be seen in Tables 8, the $k = 2$ cases have, in general, better \bar{S} scores than the $k = 3$ cases. Another interesting outcome is the very low normalized mean error (< 0.01) for all cases suggesting that clustering based on the $[s_1, s_2, s_3]$ data set yields denser, more concentrated clusters around the computed centroids.

Regardless, the most important result in this case is the strong association of observed SLSN symmetries with C_1 : $\sim 75\%$ – 76% of SLSNe-I and SLSNe-II are associated with C_1 in the CSM-I/CSM-II/MAG, $k = 2$ case. In addition, C_1 is almost entirely

Table 8
Details of the Clustering Analysis

Data Sets	Parameters	N_D^a	k	E_N	\bar{S}	C_0^b	C_1^b	C_2^b
CSM-I/CSM-II/MAG	tr_1, td_1	2	2	0.62	0.66	5.95/18.45/75.6 33.33/25.00	59.28/0.68/40.05 66.67/75.00	...
CSM-I/CSM-II/MAG	tr_1, td_1	2	3	0.46	0.58	61.11/0.00/38.89 57.14/50.00	27.70/12.16/60.14 28.57/50.00	0.00/19.05/80.95 14.29/0.00
CSM-I/CSM-II	tr_1, td_1	2	2	0.77	0.63	99.59/0.41 57.14/75.00	48.44/51.56 42.86/25.00	...
CSM-I κ /CSM-II κ /MAG	tr_1, td_1	2	2	0.68	0.65	44.61/11.03/44.36 66.67/75.00	11.19/0.00/88.81 33.33/25.00	...
CSM-I κ /CSM-II κ /MAG	tr_1, td_1	2	3	0.49	0.56	38.89/1.85/59.26 28.57/50.00	42.90/13.53/43.56 57.14/50.00	1.30/0.0/98.70 14.29/0.00
CSM-I κ /CSM-II κ	tr_1, td_1	2	2	0.66	0.57	77.18/22.82 47.62/50.00	88.76/11.24 52.38/50.00	...
CSM-I/CSM-II/MAG	s_1, s_2, s_3	3	2	<0.01	0.43	34.55/4.07/61.38 23.81/25.00	86.44/11.86/1.69 76.19/75.00	...
CSM-I/CSM-II/MAG	s_1, s_2, s_3	3	3	<0.01	0.32	26.19/4.76/69.05 28.57/25.00	82.35/17.65/0.00 71.43/75.00	71.34/2.44/26.22 0.00/0.00
CSM-I/CSM-II	s_1, s_2, s_3	3	2	<0.01	0.33	82.31/17.69 80.95/75.00	93.75/6.25 19.05/25.00	...
CSM-I κ /CSM-II κ /MAG	s_1, s_2, s_3	3	2	<0.01	0.60	31.12/5.81/63.07 42.86/25.00	73.33/26.67/0.00 57.14/75.00	...
CSM-I κ /CSM-II κ /MAG	s_1, s_2, s_3	3	3	<0.01	0.33	42.31/7.69/50.00 47.62/25.00	24.67/5.26/70.07 52.38/75.00	75.00/25.00/0.00 0.00/0.00
CSM-I κ /CSM-II κ	s_1, s_2, s_3	3	2	<0.01	0.50	84.18/15.82 38.10/25.00	73.77/26.23 61.90/75.00	...
CSM-I/CSM-II/MAG	tr_1, td_1, tr_2, td_2	4	2	0.71	0.66	2.44/18.90/78.66 38.10/25.00	60.09/0.67/39.24 61.90/75.00	...
CSM-I/CSM-II/MAG	tr_1, td_1, tr_2, td_2	4	3	0.54	0.56	0.00/16.47/83.53 19.05/0.00	61.97/0.00/38.03 52.38/50.00	26.17/13.42/60.41 28.57/50.00
CSM-I/CSM-II	tr_1, td_1, tr_2, td_2	4	2	0.84	0.63	46.77/53.23 42.86/50.00	99.59/0.41 57.14/50.00	...
CSM-I κ /CSM-II κ /MAG	tr_1, td_1, tr_2, td_2	4	2	0.77	0.64	44.81/11.14/44.05 61.90/75.00	11.56/0.00/88.44 38.10/25.00	...
CSM-I κ /CSM-II κ /MAG	tr_1, td_1, tr_2, td_2	4	3	0.57	0.54	38.18/2.42/59.39 33.33/50.00	43.88/13.61/42.52 47.62/50.00	2.41/0.00/97.59 19.05/0.00
CSM-I κ /CSM-II κ	tr_1, td_1, tr_2, td_2	4	2	0.76	0.55	88.51/11.49 61.90/75.00	77.48/22.52 38.10/25.00	...
CSM-I/CSM-II/MAG	$tr_1, td_1, tr_2, td_2, tr_3, td_3$	6	2	0.74	0.65	60.00/0.67/39.33 61.90/75.00	3.03/18.79/78.18 38.10/25.00	...
CSM-I/CSM-II/MAG	$tr_1, td_1, tr_2, td_2, tr_3, td_3$	6	3	0.57	0.55	62.11/0.26/37.63 52.38/50.00	0.00/15.48/84.52 19.05/0.00	24.66/13.70/61.64 28.57/50.00
CSM-I/CSM-II	$tr_1, td_1, tr_2, td_2, tr_3, td_3$	6	2	0.86	0.62	46.77/53.23 42.86/50.00	99.59/0.41 57.14/50.00	...
CSM-I κ /CSM-II κ /MAG	$tr_1, td_1, tr_2, td_2, tr_3, td_3$	6	2	0.80	0.64	45.11/11.03/43.86 61.90/75.00	9.79/0.00/90.21 38.10/25.00	...
CSM-I κ /CSM-II κ /MAG	$tr_1, td_1, tr_2, td_2, tr_3, td_3$	6	3	0.60	0.52	37.65/2.35/60.00 28.57/50.00	2.38/0.00/97.62 23.81/0.00	44.44/13.89/41.67 47.62/50.00
CSM-I κ /CSM-II κ	$tr_1, td_1, tr_2, td_2, tr_3, td_3$	6	2	0.82	0.54	77.18/22.82 33.33/25.00	88.76/11.24 66.67/75.00	...

Notes.

^a Normalized error (E_N) values have been rounded to two decimal points.

^b The variables C_0 , C_1 , and C_2 correspond to cluster associations with SLSN LC models and the observed SLSN sample. The top line corresponds to percentages of model data, in the same order as shown in the “Models” column, that are assigned to the cluster. The bottom line corresponds to the percentage of SLSNe-I and SLSNe-II (in the “% SLSN-I/% SLSN-II” format) that are assigned to the cluster.

composed of CSM models ($\sim 98\%$). This strengthens our previous suggestion (Section 3.3) that CSM models are superior to MAG models in reproducing the observed SLSN LC symmetry properties, including some fully symmetric LCs. The same result holds in the CSM-I κ /CSM-II κ /MAG, $k = 2$

case with more than half of observed SLSN LCs associated with the cluster that is mostly composed of CSM models. This result appears to hold up in the $k = 3$ cases. Overall, CSM and MAG models appear to be clearly distinguishable in terms of LC symmetry properties (Figure 6). This indicates that LC shape

symmetry may be critical in identifying the power input mechanism associated with observed SLSNe, based only on photometry.

5.3. $N_D = 4$

In this case, we investigate k -means clustering for the primary and the secondary rise and decline timescales. We elect to focus on the $k = 2$ cases because, again, they yield higher \bar{S} scores. Clear distinction is recovered between H-poor and H-rich CSM models in the CSM-I/CSM-II and the CSM-I κ /CSM-II κ cases: $\sim 100\%$ of H-poor CSM models constitute the C_1 data in the CSM-I/CSM-II case and $\sim 89\%$ of H-poor CSM models constitute the C_0 data in the CSM-I κ /CSM-II κ case.

For the CSM-I/CSM-II/MAG data set, we recover a cluster that is mostly composed of CSM-type models (C_1 ; 60% CSM-I/CSM-II models and 40% MAG models) and a cluster that is dominated by MAG models (C_0 ; $\sim 20\%$ CSM-I/CSM-II models and $\sim 80\%$ MAG models). The majority ($\sim 66\%$ – 75%) of SLSNe-I/SLSNe-II are associated with C_1 , indicating preference toward CSM models, although the correlation is not as strong as in the $N_D = 3$ case.

5.4. $N_D = 6$

The last clustering analysis was performed on a six-dimensional data set comprised of the primary, secondary, and tertiary rise and decline timescales. This is the most complete LC shape parameter data set we investigate because it encapsulates the three LC symmetry values, uniquely defined by their corresponding timescales. Furthermore, the use of all relevant LC shape parameters yields the highest \bar{S} scores (~ 0.8 in some cases) compared to the lower dimensionality cases. As with all other cases, we observe that $k = 2$ clustering leads to more accurate classification, therefore we only focus on these results for our discussion.

Our results are consistent with those of the $N_D = 4$ case, yielding a cluster dominated by CSM-type models (60%) and a cluster dominated by MAG models ($\sim 80\%$) with the majority of SLSNe-I/SLSNe-II associated with the former in the CSM-I/CSM-II/MAG case. In particular, $\sim 66\%$ – 75% of observed SLSN LCs are associated with the CSM-dominated cluster.

In summary, we find that clustering of LC shape properties generally favors the CSM power input mechanism although the MAG mechanism cannot be ruled out. While clustering on LC timescales supports this result, it is even more robust in the clustering of LC symmetry parameters.

6. Discussion

In this paper, we explored how high-cadence photometric observations of SLSNe detected shortly after explosion can be used to characterize their power input mechanism. In particular, we constrained the LC shape properties of a set of observed SLSNe-I and SLSNe-II, focusing only on events with complete photometric coverage and searched for possible correlations with semianalytic model LC shapes assuming either a magnetar spindown (MAG) or an SN ejecta–circumstellar matter interaction (CSM) power input (Chatzopoulos et al. 2012, 2013).

We reiterated that there is a number of simplifying assumptions in using these semianalytical models, including issues with the approximation of centrally located heating sources and homologous expansion in cases like shock heating, where the power input can occur close to the photosphere, the

assumption of constant opacity, and model parameter degeneracy (Chatzopoulos et al. 2013; Moriya et al. 2013b; Khatami & Kasen 2018). In addition, models predict bolometric LCs while the observed, rest-frame SLSN LCs are pseudo-bolometric LCs computed by fitting the SED of each event based on available observations in different filters. Regardless of all these caveats, semianalytic models still constitute a powerful tool to study SLSNe, providing us with the potential to investigate LC shape properties across the associated parameter space for each power input by computing a large number of models. Nevertheless, we have supplemented our study with data sets of numerical MAG and CSM model SLSN LCs available in the literature.

To quantitatively determine whether the main proposed SLSN power input mechanisms yield model LCs with different shape properties (rise and decline timescales and symmetry around peak luminosity), we applied k -means clustering analysis for different combinations of parameters and model data sets and computed cluster associations for the observed SLSN sample. We highlight the main results of our analysis below:

1. SLSNe exhibit a strong correlation between their primary rise (tr_1) and decline (td_1) timescales. Although this correlation is reproduced by both MAG and CSM power input models, the larger scatter found in CSM models overlaps better with the SLSN-I/SLSN-II data.
2. CSM models generally correspond to faster evolving LCs in agreement with observations of some SLSNe-I.
3. MAG models fail to produce fully symmetric LCs around peak luminosity. In particular, MAG models are never found to be symmetric around the first luminosity threshold ($s_{1,\max} = 0.54$), including in cases of high gamma-ray leakage.
4. While the majority of CSM models also fail to produce fully symmetric LC shapes, there is a small fraction of them that do. This is consistent with $\sim 24\%$ of SLSN-I LCs in our sample that are measured to be fully symmetric.
5. Symmetric SLSN LCs favor a truncated power input source that leads to faster LC decline rates past peak luminosity. The CSM model naturally provides such a framework because forward and reverse shock power inputs are terminated. An alternative truncated input could be energy release by fallback accretion.
6. MAG models fail to produce LCs with a positive second derivative during the early rise to peak luminosity (concave-up). CSM models can produce both concave-up and concave-down LCs.
7. k -means clustering analysis suggests that most observed SLSN LCs are associated with CSM power input yet the MAG model cannot be ruled out. A multiple formation channel is therefore possible for SLSNe of both spectroscopic types.
8. The most distinct clustering between MAG and CSM data is found in the 3D LC symmetry parameter space (s_1, s_2, s_3). In this case, the majority ($>75\%$) of SLSNe are strongly associated with the CSM-dominated cluster.
9. LC symmetry properties, together with the shape of the LC at early times, may be key in distinguishing between different power input mechanisms in SLSNe.

Our results illustrate the importance of early detection and high-cadence multiband photometric follow-up in determining the nature of SLSNe. As transient search surveys like LSST, ZTF, and Pan-STARRS usher in the new era of big data transient astronomy, a larger number of well-constrained SLSN LCs will become available, providing the opportunity to use photometry to characterize their power input mechanisms. This is of critical importance in the study of luminous and uncharacteristic transients in general, as photometry will be more readily available than spectroscopy in most cases.

We have shown that machine-learning approaches like k -means clustering can be instrumental in helping us characterize SLSNe based on their LC properties, namely rise and decline timescales and LC symmetry. This is made possible by comparing against the LC shape properties of different power input mechanisms using semianalytic or numerical models. As such, it is of great importance to enhance our numerical modeling efforts for all proposed power input mechanisms and survey a large fraction of the model parameter space. In addition to aiding with SLSN and luminous transient characterization and classification, this will provide us with constraints on the physical domains that enable these extraordinary stellar explosions.

We would like to thank Edward L. Robinson and J. Craig Wheeler for useful discussions and comments. We would also like to thank our anonymous referee for suggestions and comments that improved the quality and presentation of our paper. E.C. would like to thank the Louisiana State University College of Science and the Department of Physics & Astronomy for their support.

Software: Matplotlib (Hunter 2007), numpy (Oliphant 2006), SciPy (Jones et al. 2001), Scikit-learn (Pedregosa et al. 2011), SuperBol (Nicholl 2018).

ORCID iDs

E. Chatzopoulos  <https://orcid.org/0000-0002-8179-1654>

References

- Arnett, W. D. 1980, *ApJ*, 237, 541
 Arnett, W. D. 1982, *ApJ*, 253, 785
 Auchettl, K., Lopez, L. A., Badenes, C., et al. 2019, *ApJ*, 871, 64
 Barbary, K., Dawson, K. S., Tokita, K., et al. 2009, *ApJ*, 690, 1358
 Bellm, E. C., Kulkarni, S. R., Graham, M. J., et al. 2019, *PASP*, 131, 018002
 Benetti, S., Nicholl, M., Cappellaro, E., et al. 2014, *MNRAS*, 441, 289
 Bucciantini, N., Thompson, T. A., Arons, J., Quataert, E., & Del Zanna, L. 2006, *MNRAS*, 368, 1717
 Chatzopoulos, E., van Rossum, D. R., Craig, W. J., et al. 2015, *ApJ*, 799, 18
 Chatzopoulos, E., & Wheeler, J. C. 2012a, *ApJ*, 760, 154
 Chatzopoulos, E., & Wheeler, J. C. 2012b, *ApJ*, 748, 42
 Chatzopoulos, E., Wheeler, J. C., & Vinko, J. 2012, *ApJ*, 746, 121
 Chatzopoulos, E., Wheeler, J. C., Vinko, J., et al. 2016, *ApJ*, 828, 94
 Chatzopoulos, E., Wheeler, J. C., Vinko, J., Horvath, Z. L., & Nagy, A. 2013, *ApJ*, 773, 76
 Chen, K.-J., Moriya, T. J., Woosley, S., et al. 2017, *ApJ*, 839, 85
 Chen, K.-J., Woosley, S. E., & Sukhbold, T. 2016, *ApJ*, 832, 73
 Chevalier, R. A., & Fransson, C. 1994, *ApJ*, 420, 268
 Chevalier, R. A., & Fransson, C. 2003, in *Lecture Notes in Physics*, Vol. 598, *Supernovae and Gamma-Ray Bursters*, ed. K. Weiler (Berlin: Springer), 171
 Chevalier, R. A., & Irwin, C. M. 2011, *ApJL*, 729, L6
 Chomiuk, L., Chornock, R., Soderberg, A. M., et al. 2011, *ApJ*, 743, 114
 Clocchiatti, A., & Wheeler, J. C. 1997, *ApJ*, 491, 375
 Cooke, J., Sullivan, M., Gal-Yam, A., et al. 2012, *Natur*, 491, 228
 Crowther, P. A., Schnurr, O., Hirschi, R., et al. 2010, *MNRAS*, 408, 731
 De Cia, A., Gal-Yam, A., Rubin, A., et al. 2018, *ApJ*, 860, 100
 Dessart, L. 2018, *A&A*, 610, L10
 Dessart, L., & Audit, E. 2018, *A&A*, 613, A5
 Dessart, L., Audit, E., & Hillier, D. J. 2015, *MNRAS*, 449, 4304
 Dessart, L., Hillier, D. J., Audit, E., Livne, E., & Waldman, R. 2016, *MNRAS*, 458, 2094
 Dessart, L., Hillier, D. J., Waldman, R., Livne, E., & Blondin, S. 2012, *MNRAS*, 426, L76
 Dessart, L., Waldman, R., Livne, E., Hillier, D. J., & Blondin, S. 2013, *MNRAS*, 428, 3227
 Dexter, J., & Kasen, D. 2013, *ApJ*, 772, 30
 Drake, A. J., Djorgovski, S. G., Mahabal, A., et al. 2011, *ApJ*, 735, 106
 Duncan, R. C., & Thompson, C. 1992, *ApJL*, 392, L9
 Ester, M., Kriegel, H.-P., Sander, J., & Xu, X. 1996, in *Proc. Second Int. Conf. Knowledge Discovery and Data Mining, KDD'96* (AAAI Press), 226, <http://dl.acm.org/citation.cfm?id=3001460.3001507>
 Fuller, J. 2017, *MNRAS*, 470, 1642
 Gal-Yam, A. 2012, *Sci*, 337, 927
 Gal-Yam, A. 2018, arXiv:1812.01428
 Gal-Yam, A., Mazzali, P., Ofek, E. O., et al. 2009, *Natur*, 462, 624
 Gilmer, M. S., Kozyreva, A., Hirschi, R., Fröhlich, C., & Yusof, N. 2017, *ApJ*, 846, 100
 Groh, J. H., Damineli, A., Hillier, D. J., et al. 2009, *ApJL*, 705, L25
 Guillochon, J., Nicholl, M., Villar, V. A., et al. 2018, *ApJS*, 236, 6
 Guillochon, J., Parrent, J., Kelley, L. Z., & Margutti, R. 2017, *ApJ*, 835, 64
 Gvaramadze, V. V., Kniazev, A. Y., Hamann, W.-R., et al. 2010, *MNRAS*, 403, 760
 Howell, D. A., Kasen, D., Lidman, C., et al. 2013, *ApJ*, 779, 98
 Hunter, J. D. 2007, *CSE*, 9, 90
 Inserra, C., Prajs, S., Gutierrez, C. P., et al. 2018, *ApJ*, 854, 175
 Inserra, C., Smartt, S. J., Jerkstrand, A., et al. 2013, *ApJ*, 770, 128
 Ivezic, Z., Axelrod, T., Brandt, W. N., et al. 2008, *SerAJ*, 176, 1
 Jiang, Y.-F., Cantiello, M., Bildsten, L., et al. 2018, arXiv:1809.10187
 Jones, E., Oliphant, T., Peterson, P., et al. 2001, *SciPy: Open source scientific tools for Python*, <http://www.scipy.org/>
 Kaiser, N., Aussel, H., Burke, B. E., et al. 2002, *Proc. SPIE*, 4836, 154
 Kasen, D., & Bildsten, L. 2010, *ApJ*, 717, 245
 Kasen, D., Metzger, B. D., & Bildsten, L. 2016, *ApJ*, 821, 36
 Khatami, D. K., & Kasen, D. N. 2018, arXiv:1812.06522
 Kleiser, I. K. W., Kasen, D., & Duffell, P. C. 2018, *MNRAS*, 475, 3152
 Kozyreva, A., Blinnikov, S., Langer, N., & Yoon, S.-C. 2014, *A&A*, 565, A70
 Langer, N., Norman, C. A., de Koter, A., et al. 2007, *A&A*, 475, L19
 Leloudas, G., Patat, F., Maund, J. R., et al. 2015, *ApJL*, 815, L10
 Lloyd, S. 2006, *ITIT*, 28, 129
 Lunnan, R., Chornock, R., Berger, E., et al. 2013, *ApJ*, 771, 97
 Lunnan, R., Chornock, R., Berger, E., et al. 2014, *ApJ*, 787, 138
 Lunnan, R., Chornock, R., Berger, E., et al. 2016, *ApJ*, 831, 144
 Lunnan, R., Chornock, R., Berger, E., et al. 2018a, *ApJ*, 852, 81
 Lunnan, R., Fransson, C., Vreeswijk, P. M., et al. 2018b, *NatAs*, 2, 887
 MacQueen, J. 1967, in *Proc. Fifth Berkeley Symposium on Mathematical Statistics and Probability*, Vol. 1: *Statistics* (Berkeley, CA: Univ. California Press), 281, <https://projecteuclid.org/euclid.bsmsp/1200512992>
 McCrum, M., Smartt, S. J., Rest, A., et al. 2015, *MNRAS*, 448, 1206
 McDowell, A. T., Duffell, P. C., & Kasen, D. 2018, *ApJ*, 856, 29
 Metzger, B. D., Margalit, B., Kasen, D., & Quataert, E. 2015, *MNRAS*, 454, 3311
 Moriya, T. J., Blinnikov, S. I., Baklanov, P. V., Sorokina, E. I., & Dolgov, A. D. 2013a, *MNRAS*, 430, 1402
 Moriya, T. J., Blinnikov, S. I., Tominaga, N., et al. 2013b, *MNRAS*, 428, 1020
 Moriya, T. J., Nicholl, M., & Guillochon, J. 2018a, *ApJ*, 867, 113
 Moriya, T. J., Sorokina, E. I., & Chevalier, R. A. 2018b, *SSRv*, 214, 59
 Moriya, T. J., Tanaka, M., Yasuda, N., et al. 2018c, arXiv:1801.08240
 Moriya, T. J., & Tominaga, N. 2012, *ApJ*, 747, 118
 Morozova, V., Piro, A. L., & Valenti, S. 2018, *ApJ*, 858, 15
 Nche Tuma, M., Scholz, S., & Decker, R. 2009, *Business Quest Journal*, 14
 Neill, J. D., Sullivan, M., Gal-Yam, A., et al. 2011, *ApJ*, 727, 15
 Nicholl, M. 2018, *RNAAS*, 2, 230
 Nicholl, M., Berger, E., Blanchard, P. K., Gomez, S., & Chornock, R. 2019, *ApJ*, 871, 102
 Nicholl, M., Blanchard, P. K., Berger, E., et al. 2018, *ApJL*, 866, L24
 Nicholl, M., Guillochon, J., & Berger, E. 2017, *ApJ*, 850, 55
 Nicholl, M., Smartt, S. J., Jerkstrand, A., et al. 2014, *MNRAS*, 444, 2096
 Nicholl, M., Smartt, S. J., Jerkstrand, A., et al. 2015a, *MNRAS*, 452, 3869
 Nicholl, M., Smartt, S. J., Jerkstrand, A., et al. 2015b, *ApJL*, 807, L18
 Oliphant, T. 2006, *Guide to NumPy* (Trelgol Publishing), <http://www12.trelgol.org/doc/v1.10/>
 Ordovás-Pascual, I., & Sánchez Almeida, J. 2014, *A&A*, 565, A53
 Pedregosa, F., Varoquaux, G., Gramfort, A., et al. 2011, *Journal of Machine Learning Research*, 12, 2825

- Quataert, E., & Shiode, J. 2012, *MNRAS*, **423**, L92
- Quimby, R. M., Aldering, G., Wheeler, J. C., et al. 2007, *ApJL*, **668**, L99
- Quimby, R. M., Kulkarni, S. R., Kasliwal, M. M., et al. 2011, *Natur*, **474**, 487
- Rousseuw, P. J. 1987, *JCoAM*, **20**, 53
- Sako, M., Bassett, B., Becker, A. C., et al. 2018, *PASP*, **130**, 064002
- Shiode, J. H., & Quataert, E. 2014, *ApJ*, **780**, 96
- Smartt, S. J. 2009, *ARA&A*, **47**, 63
- Smith, M., Sullivan, M., D'Andrea, C. B., et al. 2016, *ApJL*, **818**, L8
- Smith, N. 2014, *ARA&A*, **52**, 487
- Smith, N., Andrews, J. E., Rest, A., et al. 2018, *MNRAS*, **480**, 1466
- Smith, N., Chornock, R., Li, W., et al. 2008, *ApJ*, **686**, 467
- Smith, N., Chornock, R., Silverman, J. M., Filippenko, A. V., & Foley, R. J. 2010, *ApJ*, **709**, 856
- Smith, N., Li, W., Foley, R. J., et al. 2007, *ApJ*, **666**, 1116
- Smith, N., Li, W., Silverman, J. M., Ganeshalingam, M., & Filippenko, A. V. 2011, *MNRAS*, **415**, 773
- Smith, N., & McCray, R. 2007, *ApJL*, **671**, L17
- Smith, N., & Owocki, S. P. 2006, *ApJL*, **645**, L45
- Sorokina, E., Blinnikov, S., Nomoto, K., Quimby, R., & Tolstov, A. 2016, *ApJ*, **829**, 17
- Sutherland, P. G., & Wheeler, J. C. 1984, *ApJ*, **280**, 282
- Valenti, S., Benetti, S., Cappellaro, E., et al. 2008, *MNRAS*, **383**, 1485
- Vreeswijk, P. M., Savaglio, S., Gal-Yam, A., et al. 2014, *ApJ*, **797**, 24
- Wachter, S., Mauerhan, J. C., Van Dyk, S. D., et al. 2010, *AJ*, **139**, 2330
- Wang, L.-J., Wang, S. Q., Dai, Z. G., et al. 2016, *ApJ*, **821**, 22
- Wheeler, J. C., Chatzopoulos, E., Vinkó, J., & Tuminello, R. 2017, *ApJL*, **851**, L14
- Woosley, S. E. 2010, *ApJL*, **719**, L204
- Woosley, S. E. 2017, *ApJ*, **836**, 244
- Woosley, S. E., Blinnikov, S., & Heger, A. 2007, *Natur*, **450**, 390
- Woosley, S. E., Eastman, R. G., Weaver, T. A., & Pinto, P. A. 1994, *ApJ*, **429**, 300
- Wozniak, P. R., Akerlof, C., Amrose, S., et al. 2001, *BAAS*, **33**, 1495
- Yan, L., Lunnan, R., Perley, D. A., et al. 2017, *ApJ*, **848**, 6
- Yan, L., Quimby, R., Ofek, E., et al. 2015, *ApJ*, **814**, 108
- Zhang, Y., & Zhao, Y. 2004, *A&A*, **422**, 1113